

The LBT Y_p Project II: MODS Spectra, Physical Conditions, and Oxygen Abundances in Local Metal-Poor Nebulae

NOAH S. J. ROGERS,¹ EVAN D. SKILLMAN,² RICHARD W. POGGE,^{3,4} ERIK AVER,⁵ MIQAELO K. WELLER,³ DANIELLE A. BERG,⁶ JOHN J. SALZER,⁷ JOHN H. MILLER, JR.,² JAYDE SPEIGEL,³ AND ALLISON L. STROM^{1,8}

¹Center for Interdisciplinary Exploration and Research in Astrophysics (CIERA), Northwestern University, 1800 Sherman Avenue, Evanston, IL, 60201, USA

²Minnesota Institute for Astrophysics, University of Minnesota, 116 Church St. SE, Minneapolis, MN 55455

³Department of Astronomy, The Ohio State University, 140 W 18th Ave., Columbus, OH, 43210

⁴Center for Cosmology & AstroParticle Physics, The Ohio State University, 191 West Woodruff Avenue, Columbus, OH 43210

⁵Department of Physics, Gonzaga University, 502 E Boone Ave., Spokane, WA, 99258

⁶Department of Astronomy, The University of Texas at Austin, 2515 Speedway, Stop C1400, Austin, TX 78712, USA

⁷Department of Astronomy, Indiana University, 727 East Third Street, Bloomington, IN 47405, USA

⁸Department of Physics and Astronomy, Northwestern University, 2145 Sheridan Road, Evanston, IL, 60208, USA

ABSTRACT

Empirically measuring the primordial He mass fraction, Y_p , requires a significant number of low-metallicity nebulae with direct constraints on He/H and O/H abundances. This technique requires high-fidelity measurements of the gas-phase physical conditions, namely the electron temperature (T_e) and density (n_e). To this end, we present deep rest-optical spectroscopy for a sample of 62 low-metallicity ($\lesssim 20\%$ solar O/H) galaxies acquired using the Multi-Object Double Spectrographs (MODS) on the Large Binocular Telescope (LBT) as part of the LBT Y_p Project. We discuss new fitting methods that recover the intensity of up to 61 H and He recombination lines, of which, up to 26 will be used to determine gas-phase He abundances, and we examine the emission line properties of the LBT Y_p Project sample. We assess different scaling relations in the low-metallicity interstellar medium (ISM), finding that $n_e[\text{Ar IV}]$ measured in 31 targets is systematically larger than $n_e[\text{S II}]$ or $n_e[\text{O II}]$. The larger densities are insufficient to significantly bias $T_e[\text{O III}]$ or the O/H abundance. $T_e[\text{S III}]$ and $T_e[\text{O III}]$ are strongly correlated over a range of $\sim 10^4$ K with very low scatter, and we calibrate new $T_e[\text{S III}]-T_e[\text{O III}]$ scaling relations for use in other low-metallicity environments. We examine different T_e measured in the low-ionization gas, finding significant scatter compared to $T_e[\text{O III}]$. The precision direct O/H derived in this analysis (median uncertainty $\sim 4\%$) are consistent with prior literature measurements, albeit with relatively large scatter. These data provide a key component necessary to empirically measure Y_p and the abundance patterns of other elements in the ISM.

Keywords: Interstellar medium (847), Chemical abundances (224), Metallicity (1031), Spectroscopy(1558)

1. INTRODUCTION

The ideal measurement of the Primordial Helium (Y_p) abundance would come from a measurement of He/H from the early universe, but the present CMB-only constraints on Y_p are relatively weak (e.g., Planck Collaboration et al. 2020). Thus, the current favored methodology follows that of M. Peimbert & S. Torres-Peimbert (1974, 1976), where the helium abundance is measured as a function of oxygen abundance and extrapolated back to an oxygen abundance of zero. It follows that robust measurements of the oxygen abundance (or some other suitable heavy element) are required in addition to the helium abundance for the determination of Y_p .

High-fidelity measurements of the O abundance are possible in the ionized phase: the rest-frame optical spectrum of H II regions and star-forming galaxies contains many strong

collisionally-excited lines (CELs) from metal ions and recombination lines of H and He. From these optical spectra, it is possible to measure the physical conditions of the electron gas, the ionic abundance of O⁺ and O²⁺, and numerous H I and He I lines necessary to constrain He/H (e.g., E. Aver et al. 2021). The optical spectra that are acquired for this analysis have many other related uses. For example, measurements of the multi-phase electron temperature (T_e) and density (n_e) structure of the interstellar medium (ISM) are used for comparing to the temperatures determined solely from H and He emission lines. Other elements (e.g., N, Ne, S, Ar) available in the optical assess systematic uncertainties related to the use of oxygen as the baseline element for comparing He abundances (V. Fernández et al. 2018). Finally, optical CELs are useful for assessing the ionizing sources within a galaxy

(e.g., J. A. Baldwin et al. 1981), which can be used to exclude nebula with significant Active Galactic Nuclei (AGN) or shock ionization where the techniques used to measure He/H are inappropriate to apply.

Therefore, a precision measurement of Y_p requires a statistically significant sample of low-metallicity galaxies with high-quality rest-frame optical and near-infrared (NIR) spectroscopy capable of measuring the physical conditions and chemical abundances in the ISM. In addition, because of the requirement of relatively high spectral resolution and a large wavelength baseline, these optical spectra are sensitive to a wealth of relatively weak lines that are not regularly detected in typical spectra collected for the purpose of nebular abundances. In this regard, these spectra share a commonality with the spectra used to obtain abundances from the very faint optical recombination lines (e.g., C. Esteban et al. 2005, 2009, 2014, 2020; E. D. Skillman et al. 2020).

To this end, the Large Binocular Telescope (LBT) Primordial He Abundance Project, hereafter LBT Y_p Project, has conducted a dedicated observing campaign to acquire optical and NIR spectroscopy of over 60 local star-forming galaxies and metal-poor H II regions. As described in E. Skillman et al. (2026, hereafter Paper I), the targets are well-known systems such as the extremely metal-poor galaxies Leo P (R. Giovanelli et al. 2013; E. D. Skillman et al. 2013), I Zw 18 (L. Searle & W. L. W. Sargent 1972; E. D. Skillman & R. C. Kennicutt 1993), and DDO 68 (F. Annibali et al. 2019), to more extreme emission line systems like Mrk 71 (R. M. Gonzalez-Delgado et al. 1994; G. Micheva et al. 2017; Y. Chen et al. 2023) and SBS0335–52E (I. I. Izotov et al. 1990; A. Wofford et al. 2021). While He/H abundances have been measured in some of these nebulae, the inhomogeneous nature of the archival observations (i.e., telescope/instrument configuration, wavelength coverage, and available H I and He I lines) results in significant systematic uncertainties when attempting to measure Y vs. O/H.

The LBT Y_p Project’s Multi-Object Double Spectrograph (MODS; R. W. Pogge et al. 2010) data provide the wavelength coverage and requisite spectral resolution to measure a plethora of T_e and n_e diagnostics. As has been demonstrated in other metal-rich nebulae (D. A. Berg et al. 2015; K. V. Croxall et al. 2016) and metal-poor galaxies (E. D. Skillman et al. 2013; F. Annibali et al. 2019; D. A. Berg et al. 2021), MODS spectra are capable of measuring T_e and n_e from ions spanning 10.4 – 40.7 eV in ionization potential (IP), which are required for determining the “direct” abundance (H. L. Dinerstein 1990; R. Maiolino & F. Mannucci 2019) of O in the multi-phase ISM. These direct abundances are relatively free of systematic uncertainties that characterize “strong-line” abundances (see L. J. Kewley & S. L. Ellison 2008; J. Moustakas et al. 2010) and provide a necessary component for determining the relation between He/H and

gas-phase metallicity. The utility of MODS for the measurement of He abundance has been illustrated in our pilot analyses of the extremely metal-poor galaxies Leo P (E. Aver et al. 2021) and AGC198691 (E. Aver et al. 2022). We now provide a homogeneous sample of low-metallicity galaxies with MODS spectroscopy, enabling the robust determination of Y_p .

A primary motivation of the LBT Y_p Project is to obtain spectra of the lowest metallicity objects to lessen the dependence on the assumption of a linear relationship between Y and O/H. In short, we would like the observations at the lowest metallicity to have the highest impact on the determination of Y_p , not the more metal-rich objects that play a dominant role in determining the slope of the Y vs. O/H relationship. Thus, as a byproduct of our new determination of Y_p , we can examine scaling relations in the metal-poor ISM, particularly between gas-phase physical conditions like T_e and n_e . While T_e scaling relations have been calibrated on the temperature trends of local star-forming regions (C. Esteban et al. 2009; L. S. Pilyugin et al. 2009; K. V. Croxall et al. 2016; K. Z. Arellano-Córdova & M. Rodríguez 2020; D. A. Berg et al. 2020; N. S. J. Rogers et al. 2021; R. J. Rickards Vaught et al. 2024), the shape of these different relations can diverge both from other empirical calibrations and from photoionization model predictions (e.g., A. Campbell et al. 1986; D. R. Garnett 1992; A. R. López-Sánchez et al. 2012). Understanding the evolution of T_e in the ISM at low-metallicity is crucial for reliable abundance surveys in the local Universe and for interpreting the emerging direct T_e in high- z galaxies observed with JWST (N. S. J. Rogers et al. 2024, 2025; E. Cataldi et al. 2025; R. L. Sanders et al. 2025; B. Welch et al. 2025). Many of these high- z galaxies also exhibit elevated n_e in the low-ionization gas (R. L. Sanders et al. 2016; A. L. Strom et al. 2017; M. W. Topping et al. 2025), and recent observations of UV emission lines in high- z extreme emission line galaxies (EELGs) indicate the presence of very high-density gas ($> 10^6$ cm $^{-3}$, see M. W. Topping et al. 2024). Deep optical spectra of low-metallicity, highly-ionized galaxies at $z=0$ assess both the density stratification in different ionization zones of the ISM and hidden high-density condensations that may bias T_e and abundance measurements (J. E. Méndez-Delgado et al. 2023b), which may be important considerations in galaxies at high z .

The format of this paper is organized as follows. In §2 we describe the MODS data reduction and analysis, ultimately delivering the H I and He I emission line fluxes and equivalent widths (EWs) for the He abundance analysis. In §3, we measure the gas-phase physical conditions, and we compare n_e measured from different ions in the ISM. We assess the T_e trends in the LBT Y_p Project nebulae in §4, providing new T_e scaling relations between T_e [O III] and T_e [S III]. In §5, we measure the total gas-phase O/H in the LBT Y_p Project sam-

ple and compare these to other direct measurements available in the literature. We summarize our conclusions in §6.

2. DATA REDUCTION AND ANALYSIS

2.1. *Observations and Reduction*

Paper I details the target selection criteria, observation setup, and aspects of the MODS data reduction up to the 1D spectra of each metal-poor nebula. While we refer the reader to this paper for these specifics, we briefly highlight the standard reduction procedure here. All science targets are observed with a $1.^{\prime\prime}0 \times 60.^{\prime\prime}0$ long slit. MODS1 and MODS2 have a spectral resolution of $R \sim 1850$ and 2300 in the blue and red channel, respectively, and a combined wavelength coverage of $3300 - 10000 \text{ \AA}$. For all data acquired within a given observing run, we use the MODSCCDRED (R. Pogge 2019) programs to process (bias subtract and flat field correct) the raw CCD images of the science targets, standard stars (at least one observed per night), and calibration lamps (observed once per run). Cosmic rays are removed from the science images using the IDL implementation of LACOSMIC (P. G. van Dokkum 2001), which are then average combined. Standard star images are median combined, where no difference in the flux calibration was observed when using an average combination of the standard star observations. The choice of standard star is made based on the time of observation in relation to the science targets and the conditions during observation.

The MODSIDL (K. V. Croxall & R. W. Pogge 2019) reduction package is used to reduce the science, standard, and lamp images, producing wavelength solutions for the 2D spectra. Standard stars are extracted and used to determine the shape of the sensitivity function for the MODS1 and MODS2 detectors. Local sky subtraction is performed using the available sky in the longslit spectrum, where the sky is modeled with a B-spline function and subtracted from the 2D science image. Science targets are extracted using a range of widths based on the slit profiles of the 2D spectra centered on $H\beta$ and $H\alpha$ for the blue and red channel, respectively. We extract every object using at least two extraction widths and check that all line ratios and physical conditions are consistent within uncertainty; when the extractions are consistent within uncertainty, we adopt the narrow extraction to reduce the RMS noise in the continuum. When wide and narrow extractions disagree, we select the wider extraction to ensure that no significant emission is omitted, except in instances where a neighboring object is affecting the flux reported for the primary target.

With the individual spectra from the MODS1 and MODS2 channels, we combine the blue and red spectra at rest-frame 5650 \AA using the SPECTRES package (A. C. Carnall 2017) to preserve the native sampling of MODS (0.5 \AA per pixel). We also examine the agreement of the blue and red spectra

around the dichroic crossover and fit a linear function to the continuum before and after 5650 \AA . In instances where there is an offset in the continua (a trend that can be produced by small differences in sky subtraction between the blue and red spectra), we apply an additive constant to the red spectrum to produce an agreement at the dichroic (9 objects in total). There are instances where the MODS2 red channel spectra are a constant factor greater than the MODS1 red channel spectra and do not align with the MODS2 blue spectra at the dichroic (8 objects in total). For these objects, we apply a multiplicative factor to the MODS2 red spectra to produce agreement at the dichroic. When MODS1 and MODS2 data are available for a given object, we combine the two using a variance-weighted average. To illustrate the quality of the MODS sample, we select a galaxy with a $F(H\beta)$ below the sample median and plot the combined MODS spectrum in Figure 1. The MODS spectrum of HS0811+4913 reveals the high signal-to-noise (S/N) detections of many faint emission lines crucial for T_e , n_e , and ionic abundance measurements.

2.2. *Emission Line Fitting*

Both the present chemical abundance analysis and the determination of He/H (E. Aver et al. 2026, hereafter Paper IV) require reliable measurements of emission lines spanning the full optical spectrum. To fit the emission lines, we split the spectrum into 18 windows and assume that the stellar continuum in each window can be approximated with a linear continuum over the small wavelength range. We do not consider areas of the continuum with significant stellar absorption in the linear continuum fit. The contribution of stellar absorption to the total Balmer line flux is accounted for via the iterative reddening correction (see §2.3).

Emission lines are generally approximated with Gaussian functions based on the combination of thermal, Doppler, and instrumental broadening of an emission line (e.g., V. Fernández et al. 2024). However, the emission line profiles observed in many of the MODS1 and MODS2 spectra are not well characterized by a Gaussian profile. This is primarily due to the targets being extended relative to the slit width and thus the instrumental profile reflects the boxcar-like nature of the slit. This presents a challenge for simultaneously fitting faint emission lines adjacent to intense lines, as exhibited in the leftmost panel of Figure 2. For example, the shape of the blended [O II] lines in HS0811+4913 is not accurately reproduced by the Gaussian emission line fits, leading to normalized residuals that can exceed 20% of the measured flux. In this case, the residuals are sufficiently large from the mismatch of the observed and fit line profiles that the weak H13 recombination line is poorly recovered.

To fit the emission lines, we adopt a super-Gaussian emission line model with functional form:

$$F_\lambda = A \times e^{-\frac{1}{2} \left(\frac{|\lambda - \lambda_0|}{\sigma_{SG}} \right)^p}, \quad (1)$$

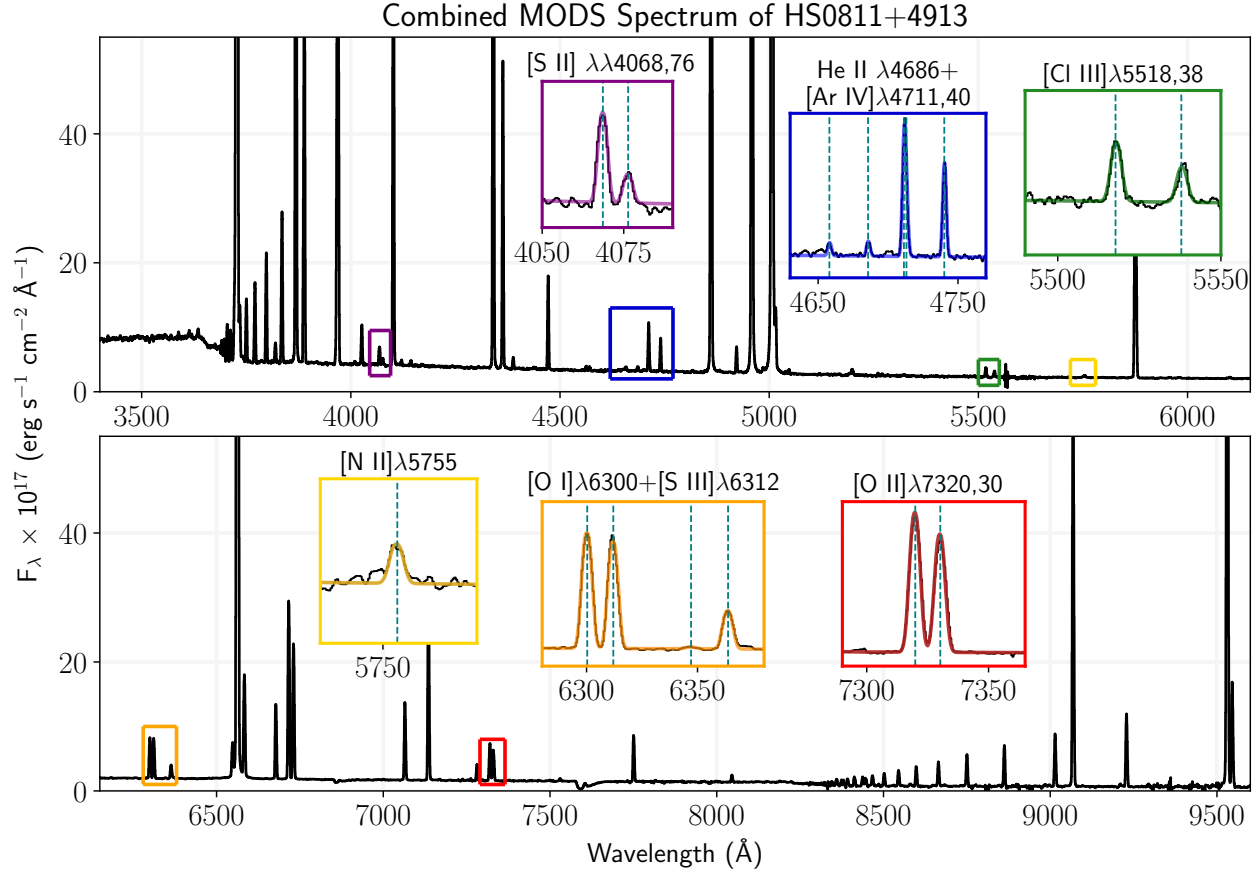


Figure 1. Combined MODS spectrum of the low-metallicity galaxy HS0811+4913. Faint T_e - and n_e -sensitive emission lines are highlighted in the subplots. The T_e -sensitive auroral line of $[\text{O III}]\lambda 4363$ is clearly visible without magnification. The spectrum shows a distinct Balmer and Paschen jump, along with numerous intense and faint He I lines crucial for the determination of He^+/H^+ .

where A is the amplitude of the super-Gaussian, λ_0 is the central wavelength of the emission line, and P is the super-Gaussian power. σ_{SG} is the width parameter of the super-Gaussian,

$$\sigma_{SG} = \frac{\text{FWHM}}{2 \times (2 \times \ln(2))^{1/P}}, \quad (2)$$

where FWHM is the Full-Width at Half Maximum of the super-Gaussian (S. Beirle et al. 2017). Assuming the emission lines can be described by Equation 1 allows for a flexible fit to the shape of the line profile, particularly the peak of the emission line. Equation 1 reduces to a Gaussian profile when $P=2$, but $P < 2$ produces a line with a sharper peak and $P > 2$ results in a flat-topped line profile. At the extremes, the line profile becomes a discontinuous peak with broad wings as $P \rightarrow 1$ and a top hat profile at $P \gg 1$.

Within each fitting window, we adopt the linear continuum model and assume all narrow lines have constant super-Gaussian FWHM, P , and wavelength offset from the theoretical wavelength, but we fit for each unique super-Gaussian amplitude. The number of free parameters, therefore, is $N+3$, where N is the number of emission lines fit within each window. We then construct a χ^2 function to mini-

mize using SCIPY (P. Virtanen et al. 2020) and determine the best-fit solution for all emission lines within the window. To calculate the emission line flux, we integrate the best-fit super-Gaussian profile over the wavelength grid of the full MODS spectrum. The super-Gaussian fit to the $[\text{O II}]$ lines of HS0811+4913 is provided in the third panel of Figure 2. The new approach reduces the normalized residuals below 10% across the full line profile and reproduces the $[\text{O II}]$ doublet, allowing for a reliable estimation of the electron density in the low-ionization gas. Further, faint lines such as H13 and H14 are well fit with the same super-Gaussian FWHM and P parameter. Note that the remaining residual at $\sim 3722 \text{ Å}$ is due to the blend of H14 with the faint $[\text{S III}]\lambda 3722$ line, the latter of which is not independently fit.

A subsample of the metal-poor nebulae show broad wings on the intense $\text{H}\beta$, $\text{H}\alpha$, and $[\text{O III}]$ optical lines. These features can further complicate the Gaussian fitting procedures, as illustrated in the second panel of Figure 2. In this example, the $\text{He I} \lambda 5016$ line flux is greatly overestimated and the normalized residuals around $[\text{O III}]\lambda 5007$ are well above 20%. This is also true for the flux of the $[\text{N II}]$ strong lines, which are faint in metal-poor galaxies and, therefore, are sensitive

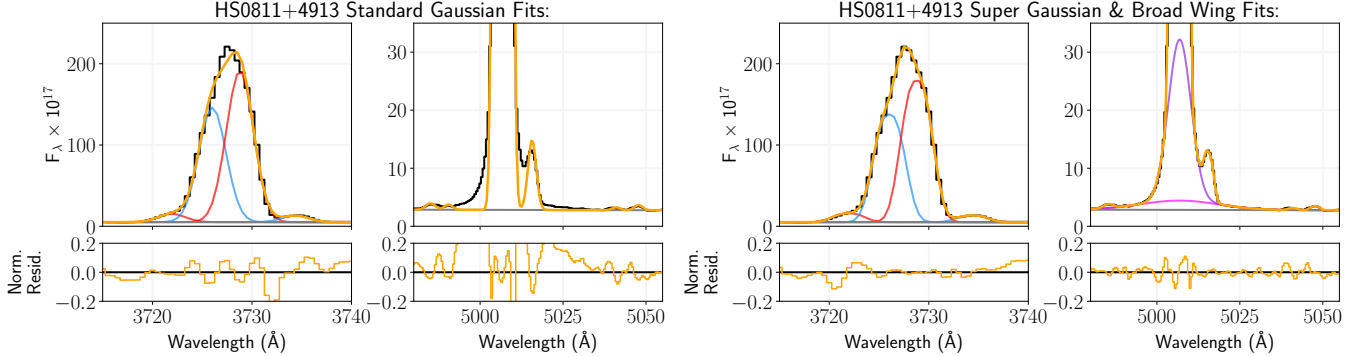


Figure 2. Examples of emission line fits in the galaxy HS0811+4913. The left two panels uses a combination of a linear continuum plus Gaussian emission line profiles to fit the H14, H13, and $[\text{O III}]\lambda\lambda 3726,29$ (first panel) and $[\text{O III}]\lambda 5007$ and $\text{He I}\lambda 5016$ (second panel). The 1D spectrum is plotted in black, the full fit is provided in orange, individual narrow emission lines are in alternating blue and red. The standard Gaussian fits have normalized residuals (lower panels) that can exceed 20%. The right two panels plot new fits using super-Gaussian profiles for the emission lines. This provides significantly better fits to the blend of H I and [O III] lines in the third panel. The inclusion of a two-component broad wing on $[\text{O III}]\lambda 5007$ (fourth panel, shown in pink and purple) provides a reliable fit to both the strong [O III] line and the faint He I line.

to how the broad component of H α is treated. The broad components may be related to high-velocity gas in the ISM, or are due to differences in the instrumental line-spread function from the assumed super-Gaussian line profile. The latter is consistent with the appearance of the broad components on the brightest emission lines. Prior LBT/MODS studies have reported the presence of such broad features in similarly metal-poor objects observed with MODS (Y. I. Izotov et al. 2017; D. A. Berg et al. 2021), and have found that the broad component generally accounts for a small fraction of the overall line flux. Given the potential diagnostic importance of He I $\lambda 5016$ and the [N II] strong lines, we model the broad wings to obtain more robust fits to both the strong lines and neighboring faint lines.

When there is clear evidence of broad emission, we follow the methodology of D. A. Berg et al. (2021) and fit the broad wing with a two-component Gaussian model. The slightly-broad Gaussian component captures slight deviations of the line profile from the narrow super-Gaussian, while the very-broad Gaussian models both deviations from the super-Gaussian profile and the contribution of high-velocity gas ($v > 1000$ km/s) that can affect the weak lines. The flux of the slightly-broad component accounts for 1-3% of the narrow component, and the narrow and slightly-broad components are added together when reporting the total line flux. The very-broad component of $[\text{O III}]\lambda 5007$ is always $< 1.5\%$ of the flux of the narrow super-Gaussian, while the broad component of H α is typically $< 2\%$ of $F(\text{H}\alpha)$ for the full sample. As this component may be associated with a high-velocity outflow that does not have the same physical conditions as the H II region, we exclude the flux of the very-broad component from the reported total line flux.

Finally, the measurements of T_e and ionic abundance are sensitive to the flux of very faint emission lines, such as auroral $[\text{O III}]\lambda 4363$ and $\text{He I}\lambda 4026$. To verify the super-

Gaussian fit, we fit faint emission lines by hand using the IRAF⁹ SPLIT routine. When there is significant disagreement between the automatic and SPLIT line fluxes, we adopt the SPLIT fluxes for our analysis. Corrections are often needed for emission lines that are close to stellar absorption features and areas in the NIR with large sky subtraction residuals, both of which can bias the linear continuum fits.

We consider three sources of uncertainty when reporting the error in emission line flux. The first, $2 \times \text{RMS} \times \sqrt{2} \times \text{FWHM}$, is related to the noise in the continuum around the emission line that could affect the super-Gaussian fit (see D. A. Berg et al. 2013). The second term is a constant 1% uncertainty, which is the minimum uncertainty determined by the level of fixed pattern noise present in the MODS detectors. The third term is the flux calibration of the MODS detectors themselves, and we refer the reader to Paper I for details regarding these response function uncertainties. In brief, MODS observations of the standard stars G191B2b and GD153 spanning three years (2021-2024) are used to derive the stability of the MODS response functions. Blue and red channel response function uncertainties are derived as a function of wavelength for both MODS1 and MODS2. We sample these functions at the observed wavelength of a given emission line to retrieve the uncertainty in the MODS flux calibration at that wavelength. This percent uncertainty is added in quadrature with the first two terms to produce the final reported line flux uncertainty. We consider an emission line detected if its S/N is above 3.

⁹ NOIRLab IRAF is distributed by the Community Science and Data Center at NSF NOIRLab, which is managed by the Association of Universities for Research in Astronomy (AURA) under a cooperative agreement with the U.S. National Science Foundation.

2.3. Reddening Correction and Emission Line Diagnostics

After emission line fitting, line fluxes and EWs of 17 H I and 9 He recombination lines are taken as inputs to the He abundance MCMC code (see Paper IV for more details). More H I and He I lines are available and fit in the MODS optical spectra (up to 31 H I lines, 28 He I lines, and 2 He II lines), but are not detected in a sufficient portion of the sample. The addition of these other H I and He I lines may help provide better constraints on the resulting He^+/H^+ abundance, but are currently not included in the Y_p analysis. The MCMC method in Paper IV solves for reddening independently, but for this analysis we use ratios of the four strongest Balmer emission lines in an iterative approach to infer $E(B-V)$ and a_H , the EW of the underlying stellar absorption in the Balmer lines. We solve for a single a_H at $\text{H}\beta$ and scale the absorption EW for $\text{H}\delta$, $\text{H}\gamma$, and $\text{H}\alpha$ based on the ratio of Balmer EWs measured from the BPASS (J. J. Eldridge & E. R. Stanway 2009; J. J. Eldridge et al. 2017; E. R. Stanway & J. J. Eldridge 2018) spectral energy distributions for young stellar populations (see E. Aver et al. 2021).

In the iterative approach, as a first pass, the theoretical $\text{H}\alpha/\text{H}\beta$, $\text{H}\gamma/\text{H}\beta$, and $\text{H}\delta/\text{H}\beta$ ratios are calculated at $T_e=10^4$ K and $n_e=10^2 \text{ cm}^{-3}$ using the atomic data of P. J. Storey & D. G. Hummer (1995). Next, the combination of $E(B-V)$ and a_H that produces agreement between the observed and theoretical ratios are determined through a χ^2 minimization using SCIPY OPTIMIZE. We use the J. A. Cardelli et al. (1989) attenuation law for the calculation of $E(B-V)$. Holding $E(B-V)$ constant, a_H is varied around the best-fit solution to determine the value at which the reduced χ^2 value increases by 1; that value is taken as the uncertainty on the underlying absorption. A similar process is done for $E(B-V)$ by holding a_H constant at the best-fit value.

With these two parameters, the spectrum is corrected for reddening, and underlying absorption is accounted for in the four strongest Balmer lines. $T_e[\text{O III}]$ is calculated using the intensity ratio of $[\text{O III}]\lambda4363/[\text{O III}]\lambda5007$, and this T_e is used to update the theoretical ratios of the H I lines. We iterate this procedure, calculating the new best-fit values for $E(B-V)$ and a_H and their associated uncertainties at each step, until the change in the measured $T_e[\text{O III}]$ is < 20 K. At the point of convergence, we use the final $E(B-V)$ to reddening correct the spectrum. We also account for a_H in the four strongest Balmer lines, and we update the lower bounds on the uncertainties for a_H such that the minimum a_H cannot go below 0 Å. The observed line fluxes and EWs required to measure Y_p are provided in Table 2, as well as the best-fit $E(B-V)$ and a_H . The uncertainty in a line intensity is determined using the line flux and reddening correction uncertainties. When reporting uncertainties on line intensity ratios, we consider the uncertainty in individual line fluxes, the error on $E(B-V)$, and the wavelength separation between the lines

of interest. This approach is also adopted when calculating physical conditions from line flux ratios of metal ions (see §3.1).

To assess the ionization conditions of the sample, we plot commonly utilized emission line ratios measured in the rest-frame optical/NIR in Figures 3 and 4. Figure 3 plots the traditional diagnostics proposed by J. A. Baldwin et al. (1981, or BPT) and S. Veilleux & D. E. Osterbrock (1987), or $[\text{O III}]/\text{H}\beta$ vs. $[\text{N II}]/\text{H}\alpha$, $[\text{S II}]/\text{H}\alpha$, and $[\text{O I}]/\text{H}\alpha$. The dashed black and dotted green lines denote the G. Kauffmann et al. (2003) and L. J. Kewley et al. (2001) demarcations for ionization from an AGN and extreme starburst galaxies, respectively. Ionized regions with line ratios above these demarcations likely have ionization sources beyond simple stellar populations, such as AGN or shocks. The line ratios measured in the LBT Y_p Project nebulae, plotted as blue diamonds, are generally offset to high $[\text{O III}]/\text{H}\beta$ and low $[\text{N II}]/\text{H}\alpha$, a pattern that is typical for high-ionization, low-metallicity nebulae (L. J. Kewley et al. 2013). Numerous galaxies have $\log([\text{O III}]/\text{H}\beta) \sim 0.3$ at $\log([\text{N II}]/\text{H}\alpha) < -2$, indicative of very low gas-phase metallicities that result in the low intensity of [O III].

For comparison, we include the emission line ratios measured in extragalactic H II regions observed as part of the CHemical Abundances Of Spirals project (CHAOS, D. A. Berg et al. 2015). We use the emission line intensities reported in D. A. Berg et al. (2020), N. S. J. Rogers et al. (2021), and N. S. J. Rogers et al. (2022). We select only H II regions with significant emission line detections for all relevant lines in each diagram. Purple circles in Figure 3 highlight the line ratios in the CHAOS H II regions, which are consistent with the trends expected for more metal-rich nebulae and softer ionizing spectra.

The CHAOS H II regions occupy clearly distinct areas of the N2-BPT diagram from the LBT Y_p Project sample, but there is some overlap between the two samples in the S2- and O1-BPT diagrams (center and right panels of Figure 3). Additionally, some nebulae fall along the L. J. Kewley et al. (2001) maximum starburst demarcation in these same diagrams, a trend that could be produced by other ionization sources in the photodissociation region (PDR) that contains low-ionization species such as O^0 and S^+ . Indeed, a small number of CHAOS H II regions also scatter above the line ratios expected for a maximum starburst, a trend that has been associated with shock ionization (K. V. Croxall et al. 2015). Shock ionization from supernovae or Wolf-Rayet (WR) stars can bias the measured gas-phase physical conditions and chemical abundances from an emission line spectrum (E. D. Skillman 1985). However, shock contribution is difficult to assess from the integrated spectra of the LBT Y_p Project nebulae beyond general emission line diagrams or the detection of emission lines from very high ionization ions

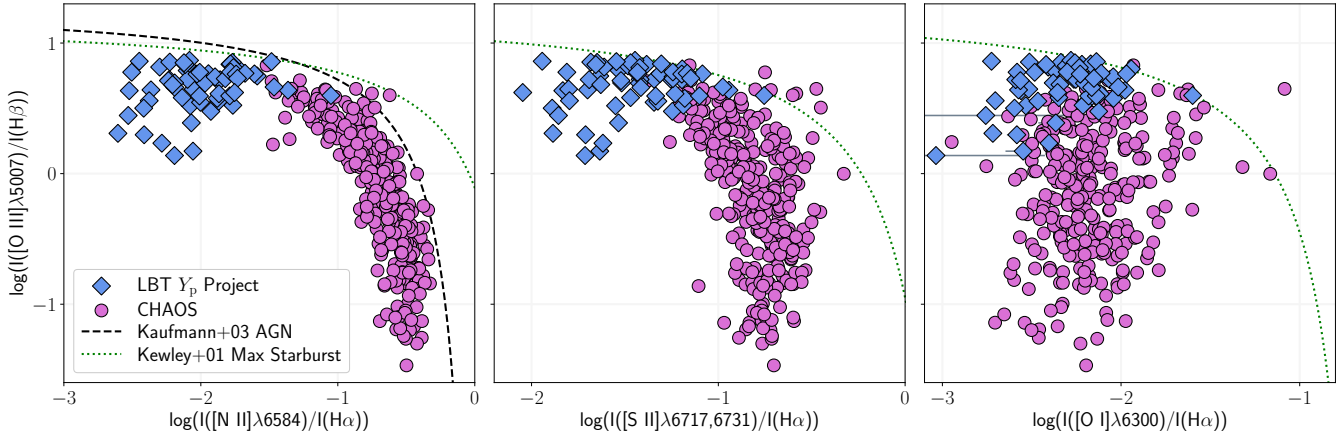


Figure 3. Emission line diagrams proposed by J. A. Baldwin et al. (1981) and S. Veilleux & D. E. Osterbrock (1987): $\log(I([O\ III]\lambda 5007)/I(H\beta))$ vs. $\log(I([N\ II]\lambda 6584)/I(H\alpha))$ (Left), $\log(I([S\ II]\lambda 6717,6731)/I(H\alpha))$ (Center), and $\log(I([O\ I]\lambda 6300)/I(H\alpha))$ (Right). Line intensity ratios measured in the LBT Y_p Project sample are plotted as blue diamonds. Line ratios measured in relatively metal-rich H II regions from the CHAOS project are plotted as purple circles for reference. The L. J. Kewley et al. (2001) and G. Kauffmann et al. (2003) demarcations proposed to distinguish between stellar and AGN ionizing sources are plotted as black dashed and green dotted lines, respectively. The LBT Y_p Project targets are characterized by highly-ionized, low-metallicity ISM and have line ratios consistent with extreme stellar ionization.

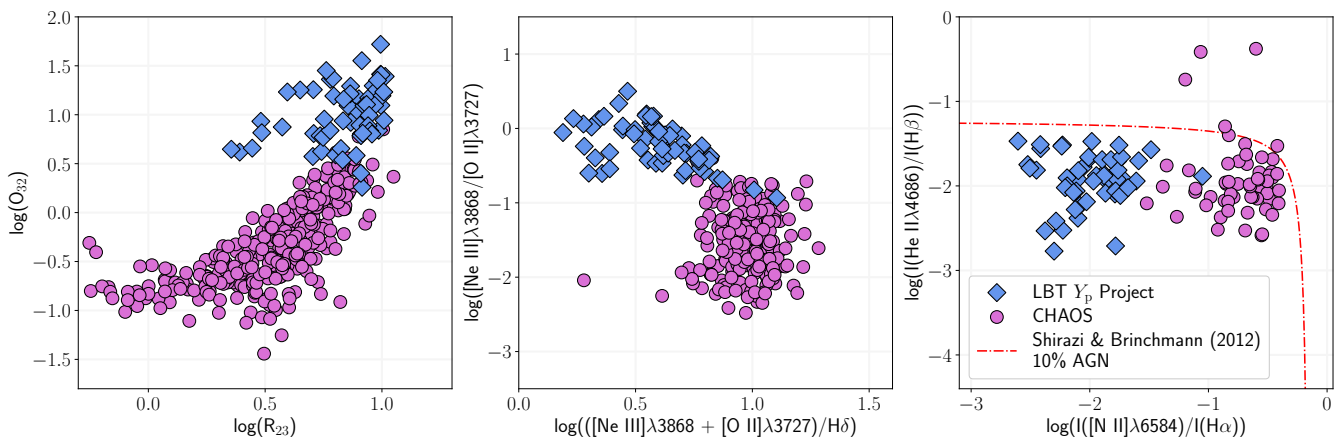


Figure 4. Additional line ratio diagrams to highlight the highly-ionized ISM of the LBT Y_p Project targets. The shape and color of each point is consistent with the labeling from Figure 3. Left: $\log(O_{32})$ vs. $\log(R_{23})$, the ionization-excitation diagram. Center: $\log(I([Ne\ III]\lambda 3869)/I([O\ II]\lambda 3727))$ vs. $\log(I([Ne\ III]) + I([O\ II])/I(H\delta))$, an alternative ionization-excitation diagram. Right: $\log(I(He\ II\ \lambda 4686)/I(H\beta))$ vs. $\log(I([N\ II]\lambda 6584)/I(H\alpha))$, a diagram to highlight nebular He II emission. The red dot-dashed line indicates line ratios from 10% AGN ionization (from M. Shirazi & J. Brinchmann 2012). All diagrams highlight the high ionization and excitation conditions observed in the targeted sample, while the line ratios remain consistent with predominantly stellar ionization.

like Ne^{4+} (Y. I. Izotov et al. 2021). While some nebulae may have significant shock contributions to these high-ionization lines (such as SHOC133, also reported by Y. I. Izotov et al. 2021), we do not attempt to correct for the shock contribution owing to the general agreement with the star-forming areas in the emission line diagrams of Figure 3.

These ionization conditions are further explored in the panels of Figure 4. In the left panel, we plot O_{32} vs. R_{23} , where $O_{32} = I([O\ III]\lambda 4959,5007)/I([O\ II]\lambda 3727)$ and $R_{23} = (I([O\ III]\lambda 4959,5007) + I([O\ II]\lambda 3727))/I(H\beta)$. While some low-metallicity nebulae have similar R_{23} as the high-metallicity H II regions, the majority of the sample contains

more highly ionized ISM and is offset to high R_{23} . The area of parameter space covered by the LBT Y_p Project targets in the ionization-excitation diagram is similar to the average conditions observed in high- z star-forming galaxies, namely $\log(O_{32}) > 0$ and $\log(R_{23}) > 0.5$ (A. E. Shapley et al. 2015, 2025; A. L. Strom et al. 2017).

A similar trend is found when plotting $\log(I([Ne\ III]\lambda 3869)/I([O\ II]\lambda 3727))$ vs. $\log(I([Ne\ III]) + I([O\ II])/I(H\delta))$ in the center panel. This diagnostic diagram has grown in popularity owing to the rest-optical observations of high- z star-forming galaxies with JWST (A. J. Cameron et al. 2023; G. Roberts-Borsani et al. 2024). Sim-

ilar to O_{32} , $\log(I([Ne\ III]\lambda3869)/I([O\ II]\lambda3727))$ traces the ionization state of the nebula via the difference in the IPs of Ne^{2+} and O^+ . The sum of [Ne III] and [O II] relative to a H I recombination line is sensitive to metallicity and, therefore, is akin to the R_{23} parameter. The low-metallicity nebulae generally have $\log(I([Ne\ III])+I([O\ II])/I(H\delta)) < 0.8$, consistent with metal-poor ISM ionized by a hard ionizing spectra. Some LBT Y_p Project targets have similar [Ne III]/[O II] intensity ratios as those observed in other high- z EELGs (e.g., [A. J. Cameron et al. 2023](#); [A. J. Bunker et al. 2023](#); [M. W. Topping et al. 2024](#); [A. E. Shapley et al. 2025](#)).

We further illustrate the presence of very high ionization conditions in the LBT Y_p Project nebulae in the right panel of Figure 4. In this panel, we plot the intensity of $He\ II\lambda4686$ relative to $H\beta$ against the $[N\ II]/H\alpha$ intensity ratio. When reporting $He\ II/H\beta$, we only consider the narrow component of $He\ II$ with FWHM similar to other neighboring emission lines ($[Fe\ III]\lambda4658$, $[Ar\ IV]\lambda4740$, etc.) and omit any broad $He\ II$ emission. However, the $He\ II$ intensity measured in the CHAOS H II regions may include a portion of broad $He\ II$ flux from, for example, WR stars ([A. R. López-Sánchez & C. Esteban 2010](#)). The red dot-dashed line from [M. Shiri & J. Brinchmann \(2012\)](#) denotes line ratio predictions when 10% of the total line flux is produced by AGN ionization. All LBT Y_p Project targets fall below this demarcation and are consistent with predominant stellar ionization. A total of 50 nebulae exhibit significant narrow $He\ II$ emission, ranging from $\sim 0.2\%$ to more than 3% the intensity of $H\beta$; however, the ionizing spectrum of simple stellar populations, even at low metallicity or when considering binary interactions, predict very few He^+ -ionizing photons ([J. J. Eldridge et al. 2017](#)). The detection of $He\ II$ in the LBT Y_p Project sample adds to an ongoing problem in nebular astrophysics, where the observed $He\ II$ emission is much larger than predicted from ionization by a stellar population alone (see discussion in [D. R. Garnett et al. 1991](#); [P. Senchyna et al. 2017](#); [D. A. Berg et al. 2021](#)). Other sources such as shocks, X-ray binaries, evolved stellar populations (i.e., WR stars, stripped stars), or AGN contamination could contribute to the production of very high-energy photons and the observed nebular $He\ II$ emission ([Y. Götberg et al. 2019](#); [P. Senchyna et al. 2020](#); [S. R. Flury et al. 2025](#); [B. Hovis-Afflerbach et al. 2025](#)). Further observations in different spectroscopic bands (UV, MIR, and NIR, see [M. Weller et al. 2026](#), hereafter Paper III) are required to further test the ionization structure and sources of these metal-poor nebulae, particularly those with similar emission line characteristics as those observed in high- z EELGs.

3. PHYSICAL CONDITIONS

3.1. n_e and T_e Calculations

We now measure the physical conditions of the ionized gas, namely T_e and n_e , in the LBT Y_p Project sample using numerous emission lines from different metal ions. To do so, we use the PYNEB package ([V. Luridiana et al. 2012, 2015](#)) version 1.1.18 and the atomic data listed in Table 1. We assume a three-zone ionization structure in each nebula, where each zone is composed of ions with similar IP and is described by a characteristic T_e . The low-ionization zone contains ions with $IP \lesssim 23$ eV, such as N^+ , O^+ , and S^+ . The ions S^{2+} , Cl^{2+} , and Ar^{2+} have $23 \lesssim IP \lesssim 35$ eV and make up the intermediate-ionization zone. Finally, we assume the high-ionization zone contains ions with $IP > 35$ eV: O^{2+} and Ar^{3+} . We note that many other ions are detected in the MODS spectra, but are not used in the present analysis of the gas-phase physical conditions (see [N. Rogers et al. 2026](#), hereafter Paper VI). In the LBT Y_p Project, the detection rate of narrow, nebular $He\ II$ is substantial: 50 objects have $He\ II\lambda4686$ detections at S/N greater than 3 (see right panel in Figure 4 and Table 2). While a fourth, very high ionization zone may be preferred for ions with $IP > 54$ eV (see [D. A. Berg et al. 2021](#)) and characterized by a T_e measurement from the [Ne III] emission lines, the [Ne III] $\lambda3342$ auroral line is not detected in a significant fraction of the sample to warrant the use of a different electron temperature.

Although CELs are sensitive to ionic abundance, T_e , and n_e , ratios of two CELs originating from the same ion eliminates the dependence on the abundance and is only sensitive to the gas-phase physical conditions. If the two emission lines are produced by energy levels of similar excitation energy but different critical densities, then the ratio is primarily sensitive to n_e . Density-sensitive line ratios that are routinely detected in the LBT Y_p Project sample are $[S\ II]\lambda6717/[S\ II]\lambda6731$, $[O\ II]\lambda3729/[O\ II]\lambda3726$, $[Cl\ III]\lambda5518/[Cl\ III]\lambda5538$, and $[Ar\ IV]\lambda4711/[Ar\ IV]\lambda4740$. The $[O\ II]\lambda3726,29$ strong lines and $[Ar\ IV]\lambda4711+He\ I\lambda4713$ are partially blended at the resolution of MODS, but the line fitting approach discussed in §2.2 allows for a constraint on n_e from these ions. Notably, the wavelength separation of the n_e -sensitive emission lines is sufficiently small such that the flux ratio is insensitive to $E(B-V)$. Therefore, we use the line flux ratios of the CELs without additionally correcting for reddening.

To measure $n_e[O\ II]$ and $n_e[S\ II]$, we apply the GETCROSSTEMDEN function along with the measured $[S\ II]$ and $[O\ II]$ line ratios and the $[N\ II]\lambda5755/[N\ II]\lambda6584$ T_e -sensitive ratio to solve for the combination of T_e and n_e required to produce the observed line ratios. If the T_e -sensitive $[N\ II]$ line ratio cannot be constrained, then we use the $[O\ III]\lambda4363/[O\ III]\lambda5007$ ratio instead, but this temperature

Table 1. Selected Atomic Data

Ion	Transition Probabilities	Collision Strengths
N^+	C. Froese Fischer & G. Tachiev (2004)	S. S. Tayal (2011)
O^+	C. Froese Fischer & G. Tachiev (2004)	R. Kisielius et al. (2009)
O^{2+}	C. Froese Fischer & G. Tachiev (2004)	P. J. Storey et al. (2014)
S^+	A. Irimia & C. Froese Fischer (2005)	S. S. Tayal & O. Zatsarinny (2010)
S^{2+}	C. Froese Fischer et al. (2006)	C. E. Hudson et al. (2012)
Cl^{2+}	P. Rynkun et al. (2019)	K. Butler & C. J. Zeippen (1989)
Ar^{2+}	C. Mendoza (1983), V. Kaufman & J. Sugar (1986)	M. E. Galavis et al. (1995)
Ar^{3+}	C. Mendoza & C. J. Zeippen (1982)	C. A. Ramsbottom & K. L. Bell (1997)

NOTE—The atomic data selected for the CELS utilized for physical conditions and O/H abundances.

does not reflect the low-ionization gas containing [O II] and [S II]. Instead, we use this estimated T_e [O III] to infer the low-ionization zone T_e , then recompute n_e [O II] and n_e [S II] at the inferred temperature. When measuring n_e [Cl III] and n_e [Ar IV], we use the GETTEMDEN function at the measured intermediate- and high-ionization zone T_e from [S III] and [O III], respectively. To estimate the uncertainty on n_e , we generate a normal distribution of 2000 line ratios with center and standard deviation equal to the measured line ratio and its uncertainty, respectively. Ratios not permitted by the atomic data are excluded, then density is recomputed from the ensemble. The standard deviation in the ensemble is used to measure the asymmetric uncertainties on n_e .

With direct constraints on n_e in multiple ionization zones, we adopt a characteristic density in the ISM that will be used for subsequent T_e and abundance calculations. Following the methods of J. E. Méndez-Delgado et al. (2023b), we prioritize different density diagnostics based on the measured n_e [S II]. When n_e [S II] < 100 cm⁻³, the ISM is in the low-density limit, where T_e and abundance calculations using optical emission lines are insensitive to n_e , so we perform all calculations at $n_e = 100 \pm 50$. If 100 cm⁻³ < n_e [S II] < 1000 cm⁻³, we use an average of n_e [S II] and n_e [O II], or n_e [S II] when the latter is unconstrained. J. E. Méndez-Delgado et al. (2023b) recommend using a combination of n_e measurements from [S II], [O II], [Fe III], [Cl III], and [Ar IV] when n_e [S II] > 1000 cm⁻³, although these high n_e [S II] are not measured in the LBT Y_p Project nebulae.

A measurement of T_e requires two CELs originating from the same ion but with a large separation in excitation energy. The following T_e -sensitive intensity ratios are possible to measure from a MODS spectrum: [N II] λ 5755/[N II] λ 6584, [O II] λ 7320,30/[O II] λ 3726,29, [O III] λ 4363/[O III] λ 5007, [Ne III] λ 3342/[Ne III] λ 3869, [S II] λ 4069,76/[S II] λ 6717,31, [S III] λ 6312/[S III] λ 9532, and [Ar III] λ 5192/[Ar III] λ 7135.

To measure T_e from one of these line ratios, we use the PYNEB GETTEMDEN function, the characteristic n_e discussed above, and the measured flux ratio of the emission lines, corrected for reddening using the $E(B-V)$ determined from §2.3. The uncertainty on $E(B-V)$ is propagated into the line flux ratio, which is dependent on the wavelength separation of the auroral and nebular emission lines; for example, the ratio of [O III] emission lines is less affected by a poorly-constrained $E(B-V)$ than the ratio of the [O II] auroral and nebular lines. Similar to density uncertainties, we generate an ensemble of 1000 line ratios using a normal distribution with center and standard deviation equal to the measured line ratio and its uncertainty, respectively. We repeat the T_e calculation for the full distribution and take its standard deviation to be the uncertainty in the measured T_e .

This general procedure is applied with a few notable caveats. First, the [O III] λ 4363 emission line can be contaminated by the neighboring [Fe II] λ 4359 (B. H. Andrews & P. Martini 2013; M. Curti et al. 2017; A. H. Khoram & F. Belfiore 2025). The contaminating [Fe II] line, if not properly accounted for, will bias the inferred T_e [O III] high and the O^{2+} abundance low, particularly in regions of high-metallicity where [Fe II] λ 4359 has been detected at comparable strengths to [O III] λ 4363 (N. S. J. Rogers et al. 2022). However, one may not expect significant [Fe II] contamination given the observational characteristics of the average nebula in this sample. For instance, the LBT Y_p Project nebulae are selected for their low gas-phase O/H, where the abundance of Fe is expected to be relatively low (roughly a factor of 55× less than the gas-phase O abundance, see J. E. Méndez-Delgado et al. 2024). Additionally, the majority of Fe should be in higher ionization states given the highly-ionized ISM (see §2.3). Nevertheless, we detect the isolated [Fe II] λ 4287 emission line in 13 nebulae; this emission line is produced by the same upper energy level as

$[\text{Fe II}]\lambda 4359$, such that the intensity ratio of the two lines is fixed at $I([\text{Fe II}]\lambda 4359)/I([\text{Fe II}]\lambda 4287) = 0.73$ (using the atomic data of [M. A. Bautista et al. 2015](#)). For nebulae with significant $[\text{Fe II}]\lambda 4287$ detections, we subtract the inferred $[\text{Fe II}]\lambda 4359$ intensity from $[\text{O III}]\lambda 4363$ before calculating $T_e[\text{O III}]$. For nebulae without significant $[\text{Fe II}]\lambda 4287$ emission, the contamination of the $[\text{O III}]$ auroral line is assumed to be negligible. The maximum magnitude of $[\text{Fe II}]$ contamination is measured in HS1222+3741 and I Zw 18 SE, where the inferred $[\text{Fe II}]\lambda 4359$ results in a 3.3% reduction in the measured $[\text{O III}]\lambda 4363$ intensity. For the 13 nebulae, the median $[\text{Fe II}]$ contamination accounts for just 1.1% of the $[\text{O III}]$ intensity; therefore, $[\text{Fe II}]$ contamination is often not a major consideration in these low-metallicity, high-ionization environments.

The second major caveat concerns contamination of the rest-NIR emission lines from the night sky. The redshift of the sample is broad, ranging from -0.00034 to 0.09193 , and these observations were conducted over many different nights with varying observing conditions (see Paper I). As such, emission lines of interest can redshift into the atmospheric O_2 A and B bands and areas of telluric absorption ([S. Noll et al. 2012](#)). While it is difficult to assess the contamination of individual emission lines, contamination of the rest-NIR $[\text{S III}]$ strong lines can be assessed using the fixed intensity ratio of the two lines, $I([\text{S III}]\lambda 9532)/I([\text{S III}]\lambda 9069) = 2.47$, and the position of known telluric features. Before calculating $T_e[\text{S III}]$, we first measure the intensity ratio of the $[\text{S III}]$ strong lines and compare to the theoretical ratio. When the ratio agrees with the theoretical ratio, we use the sum of the two strong lines to calculate $T_e[\text{S III}]$. If the ratio significantly deviates from 2.47, then telluric absorption is potentially reducing the intensity of one of the strong lines. For example, when the measured ratio is less than 2.47 we prioritize $[\text{S III}]\lambda 9069$ for $T_e[\text{S III}]$ unless it is coincident with the position of strong telluric absorption, at which point we use $[\text{S III}]\lambda 9532$. However, if the measured $[\text{S III}]$ ratio deviates by $>3\sigma$ below theory, then $[\text{S III}]\lambda 9532$ is significantly contaminated and we use $[\text{S III}]\lambda 9069$ regardless of the position of the telluric features. A similar procedure is taken for line ratios greater than theory, where $[\text{S III}]\lambda 9532$ is, generally, prioritized. Of the 58 nebulae with both $[\text{S III}]$ lines detected, 27 have $[\text{S III}]\lambda 9532/[\text{S III}]\lambda 9069$ ratios that agree with theory, 18 have ratios less than theoretical, and the remaining 13 exhibit ratios greater than theoretical. If only one $[\text{S III}]$ line is detected, then we use that emission line for $T_e[\text{S III}]$ calculation. The T_e and n_e for the LBT Y_p Project sample are reported in Table 3.

3.2. n_e Trends

Given the direct constraints on various ISM properties in the LBT Y_p Project nebulae, it is worthwhile to investigate

how physical conditions in different ionization zones scale with one another. In Figure 5, we compare the simultaneous n_e measured from four different ions, where the number of galaxies is provided in the bottom right of each panel. The most common n_e measurements are from the $[\text{O II}]$ and $[\text{S II}]$ strong lines, and the two densities plotted in the left panel show good agreement with non-negligible scatter. The Spearman correlation coefficient between $n_e[\text{S II}]$ and $n_e[\text{O II}]$ is $r = 0.54$ with a p value of 3×10^{-5} , indicating that the density measurements from the O^+ and S^+ ionization states are moderately correlated. Similar consistency between $n_e[\text{O II}]$ and $n_e[\text{S II}]$ has been reported in other samples of ionized nebulae (e.g., [J. E. Méndez-Delgado et al. 2023b](#)), and this trend may be expected if both ions reside in the same volume of the H II region.

Defining the difference between the simultaneous $n_e[\text{O II}]$ and $n_e[\text{S II}]$ in the left panel as δn_e , we find the average and standard deviation of δn_e are 56 cm^{-3} and 81 cm^{-3} , respectively. The average error on $n_e[\text{S II}]$ and $n_e[\text{O II}]$ is $\lesssim 30 \text{ cm}^{-3}$, indicating that the tendency to lower $n_e[\text{S II}]$ in the ISM and large scatter are significant. The lower $n_e[\text{S II}]$ could be related to a bias introduced to the $[\text{S II}]$ lines by Diffuse Ionized Gas (DIG) in the integrated spectrum of a galaxy's ISM. Photons with energies between 10.4 eV and 13.6 eV are sufficient to ionize S atoms, but are incapable of ionizing H or O in the ISM. Therefore, $[\text{S II}]$ emission may originate in gas both outside and within the H II region, and the DIG has lower electron density than typically observed in H II regions ([R. J. Reynolds 1991](#); [E. M. Berkhuijsen & A. Fletcher 2008](#)). This bias may be an important consideration in more distant LBT Y_p Project nebulae where the MODS longslit captures the central star-forming region and the DIG, resulting in increased scatter to lower $n_e[\text{S II}]$. Alternatively, a highly stratified ISM could result in large variations between n_e measured in the different ionization zones. For example, the ISM containing O^+ also contains S^+ , S^{2+} , Cl^{2+} , and Ar^{2+} owing to the high IP of O^+ . Should the electron density be larger near the ionizing sources and in the ISM with higher-ionization ions, then the $n_e[\text{O II}]-n_e[\text{S II}]$ trends may be the result of a stratified ISM.

This can also be assessed with density measurements from other high-ionization ions in the LBT Y_p Project nebulae. The next two panels of Figure 5 plot $n_e[\text{S II}]$ against the intermediate- and high-ionization zone densities from $[\text{Cl III}]$ and $[\text{Ar IV}]$, respectively. Owing to the faint lines and the increased noise near the dichroic crossover in the MODS detectors at $\sim 5700 \text{ \AA}$, there are few nebulae where $n_e[\text{Cl III}]$ can be reliably constrained. However, the CELs of $[\text{S II}]$ and $[\text{Ar IV}]$ are significantly detected in 31 nebulae, allowing for a comparison of the low- and high-ionization zone densities. The average $n_e[\text{Ar IV}]$ plotted in the right panel of Figure 5 is $\sim 1500 \text{ cm}^{-3}$, showing a clear trend of increasing

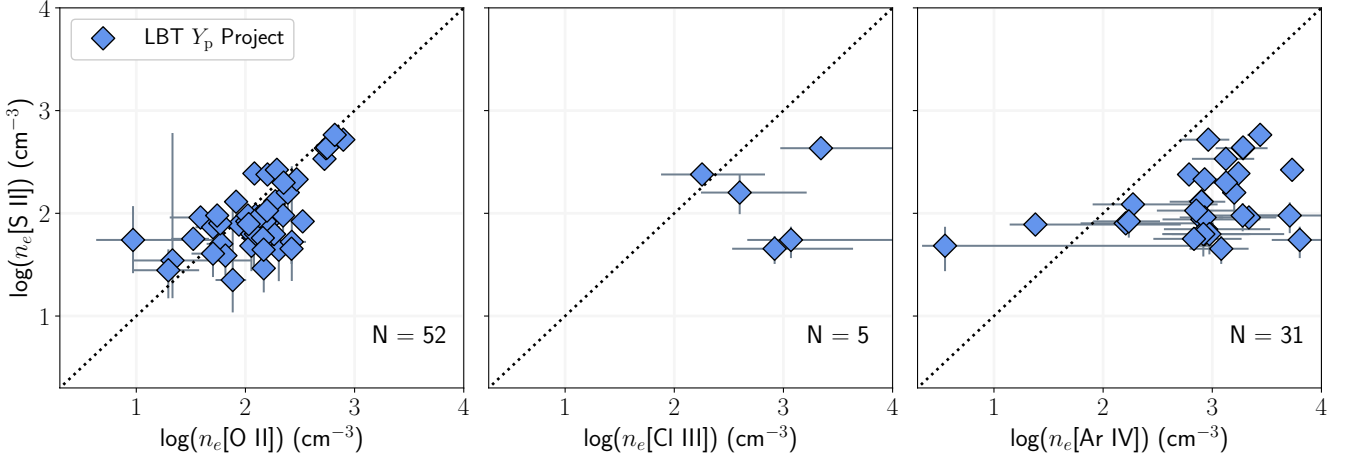


Figure 5. Direct density trends measured in the LBT Y_p Project sample. $n_e[\text{S II}]$ is plotted against $n_e[\text{O II}]$ in the low-ionization zone (Left), $n_e[\text{Cl III}]$ in the intermediate-ionization zone (Center), and $n_e[\text{Ar IV}]$ in the high-ionization zone (Right). The dotted black line represents equivalent densities. The number of nebulae with simultaneous n_e is provided in the bottom right of each panel. The [S II] and [O II] densities scatter around the one-to-one line, but $n_e[\text{Cl III}]$ and $n_e[\text{Ar IV}]$ are systematically higher than the low-ionization zone densities.

n_e with ionization state and corroborating density trends reported in other EELGs from optical (D. A. Berg et al. 2021; J. E. Méndez-Delgado et al. 2023b) and UV CELs (M. Mingozi et al. 2022; M. W. Topping et al. 2025).

An important caveat to these findings is that the [S II] and [Ar IV] line intensity ratios are sensitive to n_e in different regimes. The critical density of [S II] $\lambda 6717$ at 1.75×10^4 K is 1500 cm^{-3} , such that the [S II] line ratio is most sensitive to density above 10^2 cm^{-3} and below $\sim 1.5 \times 10^3 \text{ cm}^{-3}$. The [Ar IV] line ratio is sensitive to n_e between $\sim 10^3$ and 10^5 cm^{-3} . The difference in critical densities may contribute to the offset observed in the $n_e[\text{S II}]-n_e[\text{Ar IV}]$ panel of Figure 5. This can be assessed using the auroral lines of [S II] to recompute n_e ; as J. E. Méndez-Delgado et al. (2023b) discuss, the [S II] and [O II] auroral-to-nebular line ratios are sensitive to n_e up to $\sim 10^5 \text{ cm}^{-3}$ due to the high critical densities of the energy levels that produce auroral [O II] and [S II] emission. To assess if higher n_e is masked by the nebular [O II] and [S II] ratios, we redetermine $n_e[\text{O II}]$ and $n_e[\text{S II}]$ using the $[\text{O II}]\lambda 7320,30/[\text{O II}]\lambda 3727$ and $[\text{S II}]\lambda 4069,71/[\text{S II}]\lambda 6717,31$ ratios, respectively. This requires an independent measure of T_e , so we assume a fixed low-ionization zone T_e (either the measured $T_e[\text{N II}]$ or using a T_e scaling relation, see discussion in §5.1).

In Figure 6, the resulting auroral-to-nebular n_e are plotted against the standard n_e calculated from the nebular lines only. The blue diamonds and green circles are calculated using the line ratios from [S II] and [O II], respectively. Consistent with J. E. Méndez-Delgado et al. (2023b), we find that the auroral-to-nebular [O II] ratios indicate values of n_e moderately higher than the nebular lines alone, assuming the characteristic low-ionization zone T_e is reflective of the gas containing O^+ and S^+ . The [S II] auroral-to-nebular line ratios produce large scatter in n_e , which may be the result of a different T_e in the S^+ gas that deviates from the assumed low-

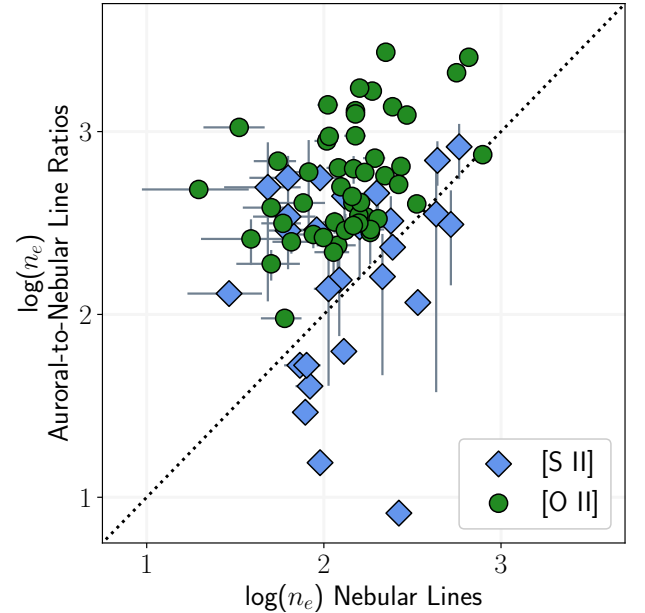


Figure 6. Electron density measured in the LBT Y_p Project nebulae from the [O II] (green circles) and [S II] emission lines (blue diamonds). The horizontal axis represents n_e measured from the nebular line ratios $[\text{O II}]\lambda 7329/[\text{O II}]\lambda 3726$ and $[\text{S II}]\lambda 6731/[\text{S II}]\lambda 6717$. The vertical axis represents n_e measured from the auroral-to-nebular line ratios $[\text{O II}]\lambda 7320,30/[\text{O II}]\lambda 3727$ and $[\text{S II}]\lambda 4069,76/[\text{S II}]\lambda 6717,31$ assuming a fixed low-ionization zone T_e . In general, the [O II] and [S II] auroral line ratios suggest larger n_e than the nebular lines alone. The higher densities lead to increased collisional de-excitation of the [O II] and [S II] nebular lines which can, potentially, bias electron temperature and ionic abundance calculations.

tios produce large scatter in n_e , which may be the result of a different T_e in the S^+ gas that deviates from the assumed low-

ionization zone T_e . The average $n_e[\text{O II}]$ and $n_e[\text{S II}]$ increase to $705 \pm 84 \text{ cm}^{-3}$ and $276 \pm 42 \text{ cm}^{-3}$, respectively, which is larger than implied from the nebular lines alone but still less than the average [Ar IV] densities.

Significant density stratification could systematically bias the T_e and ionic abundances, which assume the characteristic ISM density discussed in the previous section. Of upmost importance is collisional de-excitation of [O III] $\lambda 5007$, which originates from an upper energy level with critical density of $\sim 8 \times 10^5 \text{ cm}^{-3}$ at $T_e = 1.75 \times 10^4 \text{ K}$. If $n_e[\text{Ar IV}]$ is appropriate for the high-ionization zone and the marginal collisional de-excitation in [O III] $\lambda 5007$ is not considered, then $T_e[\text{O III}]$ could be biased high and produce low O²⁺/H⁺ (Z. Martinez et al. 2025). Further, the larger n_e in Figure 6 measured from the auroral-to-nebular line ratios of [S II] and [O II] will increase the ionic abundance of O⁺. The net result of these two affects is a potentially different total O/H abundance that could alter the He/H vs. O/H relation.

To assess whether these higher densities should be considered, we repeat the $T_e[\text{O III}]$ and O²⁺ ionic abundance calculations using $n_e[\text{Ar IV}]$ when available, then recompute O⁺ using the higher characteristic n_e inferred from the [O II] and [S II] auroral-to-CEL ratio and the low-ionization zone T_e . In all but one case¹⁰, adopting the higher ISM densities produces a fractional change to the total O/H abundance that is less than the average uncertainty in O/H ($\sim 4\%$ for the full LBT Y_p Project sample). Therefore, considering higher n_e does not produce a meaningful change in the total O/H in the LBT Y_p Project nebulae, and we proceed with the characteristic n_e discussed in §3.1. Only direct measurements of n_e in the different ionization zones can assess the presence of very high-density gas, which will strongly affect chemical abundance measurements in high-z EELGs with n_e in excess of 10^6 cm^{-3} (e.g., M. W. Topping et al. 2024; M. J. Hayes et al. 2025).

4. TEMPERATURE SCALING RELATIONS

With the wealth of T_e information available from this sample of ionized regions, we now provide empirical constraints on the trends of T_e as measured from different ions within the same nebula. These T_e scaling relations, often referred to as T_e - T_e relations, are crucial for typical direct abundance studies: when an ionization zone temperature is missing, these T_e scaling relations can be used to infer the missing T_e for chemical abundance calculations in the ionization zone of interest. T_e scaling relations have been calibrated via two methods, the first of which utilizes empirical direct T_e data

from large samples of individual ionized regions (C. Esteban et al. 2009; K. V. Croxall et al. 2016; R. M. Yates et al. 2020; N. S. J. Rogers et al. 2021; J. E. Méndez-Delgado et al. 2023b; D. Scholte et al. 2026) or from spaxels of IFU observations in star-forming galaxies (R. J. Rickards Vaught et al. 2024; A. H. Khoram & F. Belfiore 2025). Obtaining a statistically-significant sample of direct T_e measurements from multiple ions is observationally challenging, requiring a combination of high sensitivity and broad wavelength coverage to detect the auroral emission lines and their strong line counterparts, respectively. The second method of calibrating T_e scaling relations circumvents these problems by utilizing photoionization models to predict the trend of T_e in different ionization zones over a range of model ionization parameters and metallicities (A. Campbell et al. 1986; D. R. Garnett 1992; B. E. J. Pagel et al. 1992; Y. I. Izotov et al. 2006b). The functional form of the T_e scaling relations has a profound impact on chemical abundance measurements when direct T_e data are missing, and the ionized nebulae in this study present an opportunity to recalibrate these relations at high T_e /low metallicity.

4.1. $T_e[\text{S III}]-T_e[\text{O III}]$

$T_e[\text{O III}]$ is measured in every target, and the next most common T_e measurement is made from [S III] $\lambda 6312$. Only two galaxies, AGC198691 and HSCJ2314+0154, lack a significant detection of the [S III] auroral line. The low excitation energy of the [S III] $^1\text{S}_0$ level, 3.37 eV, relative to other commonly-utilized auroral lines (e.g., [O III] $\lambda 4363$ at 5.35 eV) makes this line relatively easy to detect in both low- and high-metallicity nebulae (e.g., K. V. Croxall et al. 2016). If, empirically, $T_e[\text{S III}]$ and $T_e[\text{O III}]$ trace one another over a broad range in T_e , then the [S III] auroral line may offer a reliable method to infer the temperature of the [O III] emitting region when [O III] $\lambda 4363$ is not detected. In Figure 7, we plot the $T_e[\text{O III}]-T_e[\text{S III}]$ trends measured in 60 low-metallicity nebulae as blue diamonds. The black dotted line represents equivalent T_e as measured from the two ions. There is a tight correlation between the intermediate- and high-ionization zone temperatures at $1.1 \times 10^4 \text{ K} < T_e[\text{O III}] < 2.1 \times 10^4 \text{ K}$, indicating that these two T_e are related to one another in the ISM.

Three T_e scaling relations are plotted: the D. R. Garnett (1992) photoionization model relation in dashed red, the N. S. J. Rogers et al. (2021) empirical calibration derived from high-metallicity H II regions in dot-dashed orange (plotted over the range of T_e observed in the CHAOS H II regions), and the D. Scholte et al. (2026) relation measured from T_e trends in 3781 galaxies in the Dark Energy Spectroscopic Instrument (DESI, DESI Collaboration et al. 2024) survey in solid purple. With the large number of homogeneous T_e , we derive a new $T_e[\text{S III}]-T_e[\text{O III}]$ scaling relation using the

¹⁰ The one galaxy where the change in O/H is significant is WJ0851+5841, where an increase in the adopted n_e by more than a factor of 8 and 5 in the low- and high-ionization zones, respectively, produces a 7% larger O/H.

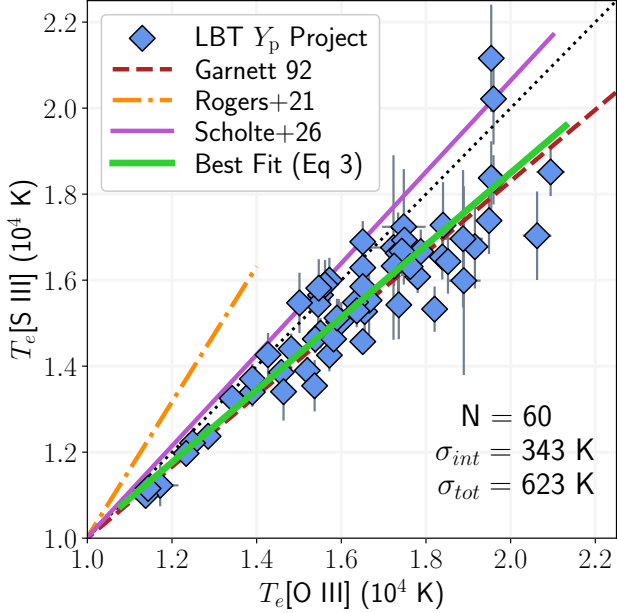


Figure 7. Simultaneous $T_e[\text{S III}]$ and $T_e[\text{O III}]$ measured from 60 LBT Y_p Project targets are plotted in blue. The black dotted line represents equivalent temperatures. The red dashed line is the photoionization model T_e scaling relation from D. R. Garnett (1992), the empirical scaling relations derived by N. S. J. Rogers et al. (2021) and D. Scholte et al. (2026) are provided as the dot-dashed orange and solid purple lines, respectively. The best-fit scaling relation to the low-metallicity nebulae (green solid line) is similar to the photoionization model T_e scaling relation. While small compared to the uncertainties on $T_e[\text{S III}]$, the intrinsic and total dispersion in the empirical T_e about this relation (provided in the bottom right) are non-negligible.

approach of N. S. J. Rogers et al. (2021). In brief, we use the SCIPY implementation of Orthogonal Distance Regression (ODR) to fit a linear relation to the T_e data considering the uncertainties on both $T_e[\text{S III}]$ and $T_e[\text{O III}]$. We then use the best-fit parameters from the ODR fit in the PYTHON LINMIX package¹¹, which is based on the IDL fitting routine of B. C. Kelly (2007), to determine the intrinsic random dispersion, σ_{int} , in the dependent variable about the line of best fit. The total scatter in T_e , σ_{tot} , about the relation is determined using the formulation outlined in A. G. Bedregal et al. (2006), and this is provided in the lower right of Figure 7. We repeat this process for the inverse relation to determine the random and total dispersion in the other T_e , which is not necessarily the same due to the asymmetric uncertainties on $T_e[\text{S III}]$ and $T_e[\text{O III}]$ (see discussion in N. S. J. Rogers et al. 2021). The best-fit relation for the $T_e[\text{S III}]-T_e[\text{O III}]$ trend is plotted in

Figure 7 as a green solid line and has the functional form

$$T_e[\text{S III}] = 0.84(\pm 0.04) \times T_e[\text{O III}] + 1700(\pm 600) \text{ K} \quad (3)$$

$$\sigma_{int} = 340 \pm 90 \text{ K.}$$

The inverse relation, which could be used to infer $T_e[\text{O III}]$ from a measured $T_e[\text{S III}]$, is described by

$$T_e[\text{O III}] = 1.19(\pm 0.06) \times T_e[\text{S III}] - 2000(\pm 800) \text{ K} \quad (4)$$

$$\sigma_{int} = 420 \pm 110 \text{ K.}$$

When applying these T_e relations to infer a missing T_e , we recommend adding σ_{int} in quadrature to the propagated uncertainty of the measured T_e (see Eq. 8 in N. S. J. Rogers et al. 2021). This approach reflects the limitations of the linear T_e scaling relations to match the empirical, random scatter in the temperature trends of ionized nebulae.

The empirical T_e data and scaling relations of Equations 3 and 4 agree remarkably well with the photoionization model predictions of D. R. Garnett (1992), consistent with findings from other direct abundance studies (e.g., J. Kennicutt et al. 2003; B. E. Miranda-Pérez & A. M. Hidalgo-Gámez 2023). However, this relation diverges from the empirical measurements made in N. S. J. Rogers et al. (2021) and D. Scholte et al. (2026), both of which find that a steeper slope describes the $T_e[\text{S III}]-T_e[\text{O III}]$ scaling relation. The majority of the H II regions used in calibrating the N. S. J. Rogers et al. (2021) empirical relations have $T_e \lesssim 10^4$ K, indicating that a different functional form may be necessary for more metal-rich/cool nebulae. This is qualitatively supported by the DESI data, where the highest density of galaxies in D. Scholte et al. (2026) have $10^4 \text{ K} < T_e[\text{O III}] < 1.4 \times 10^4$ K, and the best-fit relation has a slope closer to unity. The LBT Y_p Project nebulae at $T_e[\text{O III}] < 1.4 \times 10^4$ K also have $T_e[\text{O III}] \approx T_e[\text{S III}]$, which is similar to the D. R. Garnett (1992) relation predictions in this temperature range. The T_e scaling relations provided in Equations 3 and 4 are only applicable over their calibration range, $\sim 1.1 < T_e[\text{O III}]/10^4 \text{ K} < 2.1$, but argue for a shallow slope in $T_e[\text{S III}]-T_e[\text{O III}]$.

Another striking feature is the low intrinsic dispersion about the best-fit relation. $T_e[\text{S III}]$ has been observed to tightly correlate with $T_e[\text{N II}]$ in high-metallicity nebulae (e.g., D. A. Berg et al. 2020), but the scatter in $T_e[\text{S III}]-T_e[\text{O III}]$ measured from the same nebulae is typically $\sigma_{int} \sim 830-1110$ K (N. S. J. Rogers et al. 2021; J. E. Méndez-Delgado et al. 2023b; D. Scholte et al. 2026). The intrinsic dispersion in Figure 7 is now comparable to the uncertainty on individual $T_e[\text{O III}]$ measurements, indicating that the intermediate and high-ionization zone temperatures are strongly related in the metal-poor ISM. A potential cause for the enhanced scatter in T_e at high metallicities is contamination of the [O III] auroral line by [Fe II] emission, although spectroscopic samples of extragalactic H II regions

¹¹ <https://github.com/jmeyers314/linmix>

have found that [Fe II] contamination is infrequent (N. S. J. Rogers et al. 2022; R. J. Rickards Vaught et al. 2024).

An alternative explanation for the additional scatter in $T_e[\text{S III}]-T_e[\text{O III}]$ in metal-rich nebulae is a biased high-ionization zone temperature due to significant T_e fluctuations within the ISM. In the presence of T_e inhomogeneities, auroral line intensities are elevated and produce erroneously high T_e when calculated under the assumption of uniform gas temperature (M. Peimbert 1967). However, observationally constraining the magnitude of T_e fluctuations, which is parameterized by the value t^2 , requires the detection of extremely faint metal recombination lines in the rest-optical (e.g., C. Esteban et al. 2004, 2009, 2020; L. Toribio San Cipriano et al. 2016; E. D. Skillman et al. 2020) or the T_e -insensitive infrared fine-structure lines (C. Lamarche et al. 2022; Y. Chen et al. 2023). The former are particularly challenging to detect in metal-poor nebulae, as the intensity of metal recombination lines scales with the abundance of the ion. However, our sample includes multiple O II recombination line detections that are blended at the resolution of MODS. Direct constraints on the temperature structure and t^2 within these metal-poor nebulae may be possible with followup observations on higher-resolution optical spectrographs or with infrared observations to detect the metal fine-structure lines.

Recently, J. E. Méndez-Delgado et al. (2023a) found that the magnitude of t^2 is correlated with the difference between $T_e[\text{N II}]$ and $T_e[\text{O III}]$; under a simple geometric assumption of a H II region, this trend may be related to larger T_e fluctuations near the ionizing sources within the high-ionization zone. Additionally, they find that metal-poor, high-ionization nebulae similar to those in the LBT Y_p Project are characterized by larger t^2 , although only one extragalactic H II region in their sample has $T_e[\text{O III}] > 1.6 \times 10^4$ K. The detection rate of the [N II] auroral line is relatively low in the LBT Y_p Project sample (see following subsection), so we cannot apply the J. E. Méndez-Delgado et al. (2023a) relation to infer t^2 for the majority of the targets. If strong T_e fluctuations are universally present in the nebulae, then one may expect $T_e[\text{O III}]$ to be biased high relative to the predictions of the D. R. Garnett (1992) trend, as the photoionization model T_e scaling relation is calibrated on the ion-weighted electron temperature and not the model line ratio temperatures. However, this does not mean the present sample is described by negligible t^2 . Rather, temperature fluctuations may affect $T_e[\text{O III}]$ to a lesser extent than predicted by Eq 4 of J. E. Méndez-Delgado et al. (2023a), or that these variations also affect the measurement of $T_e[\text{S III}]$ in the highly-ionized, high- T_e ISM. To fully explore the shape of and scatter around the $T_e[\text{S III}]-T_e[\text{O III}]$ will require a larger sample of H II regions that span a range of T_e lower than those measured in the LBT Y_p Project, but that is beyond the scope of the present analysis.

4.2. $T_e[\text{O III}]$ and Low-Ionization Zone Temperatures

The next most common auroral line detections are from [O II] and [S II], with 55 and 45 significant detections, respectively. We also detect the [N II] $\lambda 5755$ auroral line in 20 targets, significantly less than the number of [O II] auroral line detections owing to the low gas-phase N abundance and overall high ionization conditions in the ISM of low-metallicity star-forming galaxies. The T_e trends of these three ions are plotted against $T_e[\text{O III}]$ in Figure 8, where the color coding of the T_e scaling relations are the same as used in Figure 7. We have also included the T_e scaling relation of B. E. J. Pagel et al. (1992) as the purple dot-dashed line. We extrapolate these T_e relations beyond their calibration range to assess the trends in the low-metallicity ISM. The left panel reveals that the $T_e[\text{O III}]-T_e[\text{N II}]$ distribution generally follows the scaling relations of D. R. Garnett (1992) and N. S. J. Rogers et al. (2021); of the 20 nebulae with simultaneous $T_e[\text{N II}]$ and $T_e[\text{O III}]$, all but two have $T_e[\text{O III}] \geq T_e[\text{N II}]$. We do not attempt to calibrate a new T_e scaling relation due to the paucity of simultaneous $T_e[\text{N II}]$ and $T_e[\text{O III}]$ measurements.

The galaxies SHOC133 and WJ1205+4551 have a $T_e[\text{N II}]$ that is ~ 2000 K greater than the measured $T_e[\text{O III}]$ temperature. Both galaxies were observed by Y. I. Izotov et al. (2021), where SHOC133 is labeled therein as J0240–0828. In agreement with the previous observations, both SHOC133 and WJ1205+4551 show evidence of very high-ionization emission such as narrow He II $\lambda 4686$, [Ne V] $\lambda 3426$, and [Fe V] $\lambda 4227$. Our measurements of $T_e[\text{O III}]$ are in fairly good agreement with those reported in Y. I. Izotov et al. (2021), but there are no reported $T_e[\text{N II}]$ in the prior observations of either galaxy. The MODS spectrum of SHOC133 also exhibits sharp line profiles with narrow super-Gaussian power $P \lesssim 1.7$. Additionally, other studies have reported the detection of NIR coronal lines in WJ1205+4551 (A. Aravindan et al. 2024); while the coronal lines of [Fe X] are undetected in the LBT Y_p Project MODS spectra of WJ1205+4551, there is a tentative detection of [Fe VIII] $\lambda 6087$ (in agreement with Y. I. Izotov et al. 2021). It is interesting to note that the $T_e[\text{S III}]$ in these galaxies are also greater than the measured $T_e[\text{O III}]$, indicating an inverted T_e structure relative to the predictions from photoionization models at low gas-phase metallicity. Given the evidence from these spectral features and the inverted T_e structure in the ISM, it is possible that other ionization sources significantly contribute to the CELs of SHOC133 and WJ1205+4551, despite their strong line ratios being indicative of an ionizing spectrum powered by stars.

With the exception of these two galaxies, the low-metallicity nebulae of the LBT Y_p Project show $T_e[\text{O III}] \gtrsim T_e[\text{N II}]$ when the faint [N II] auroral line is detected. This is not the case for the temperature trends of $T_e[\text{O III}]$ vs. $T_e[\text{O II}]$ and $T_e[\text{S II}]$, which are plotted in the center and right panels

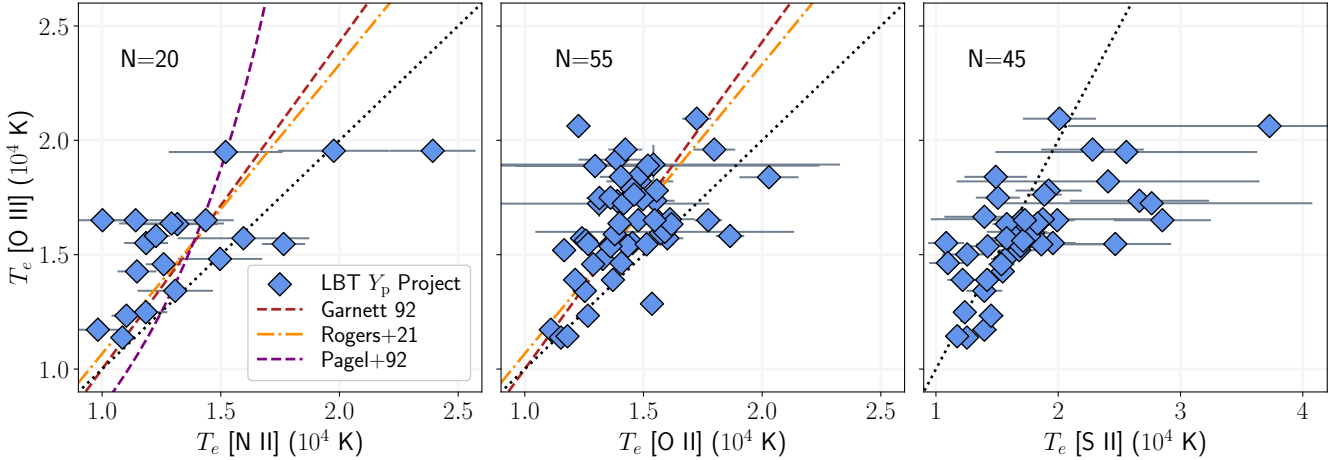


Figure 8. A comparison of $T_e[\text{O III}]$ in the LBT Y_p Project sample to T_e from the low-ionization emission lines of [N II] (Left), [O II] (Center), and [S II] (Right). The T_e scaling relations of D. R. Garnett (1992), B. E. J. Pagel et al. (1992), and N. S. J. Rogers et al. (2021) are plotted as red dashed, purple dot-dashed, and orange dashed lines, respectively. The black dotted line represents equivalent temperatures. The number of nebulae with simultaneous T_e detections is provided in the upper left of each panel. The $T_e[\text{O III}]-T_e[\text{N II}]$ and $T_e[\text{O III}]-T_e[\text{S II}]$ show substantial scatter to higher $T_e[\text{O II}]$ and $T_e[\text{S II}]$ relative to $T_e[\text{O III}]$.

of Figure 8, respectively. Prior studies have found large dispersion in empirical $T_e[\text{O III}]-T_e[\text{O II}]$ data (J. Kennicutt et al. 2003; D. A. Berg et al. 2020; R. M. Yates et al. 2020; D. Scholte et al. 2026), and the standard deviation around the D. R. Garnett (1992) relation observed in the LBT Y_p Project $T_e[\text{O II}]$ is ~ 2600 K. While 17 nebulae have simultaneous $T_e[\text{O III}]$ and $T_e[\text{O II}]$ that agree with the D. R. Garnett (1992) scaling relation, $T_e[\text{O II}]$ in 13 nebulae are greater than predicted by the scaling relation by more than 2σ . This scatter could be influenced by several mechanisms; for example, the [O II] auroral lines can redshift into the atmospheric A band at ~ 7590 - 7710 Å, but this would result in lower auroral line intensity and bias $T_e[\text{O II}]$ low. We have already removed any nebulae that show significant absorption around the [O II] auroral lines from Figure 8, although increased night sky residuals in the NIR can complicate the auroral line detection and fitting for some of the nebulae.

The ^2P levels of the O^+ ion can be populated by recombination, resulting in increased $[\text{O II}]\lambda 7320,30$ emission and an erroneously high $T_e[\text{O II}]$ if the ^2P levels are assumed to be populated purely by collisional excitation (R. H. Rubin 1986; X. W. Liu et al. 2001). Equation 2 in X. W. Liu et al. (2000) provides a means to account for the dielectronic recombination contribution of the [O II] auroral line intensity relative to $\text{H}\beta$. We apply this equation to the subsample of nebulae with significant [O II] auroral line detections and find that the average correction for dielectronic recombination is a $< 3\%$ reduction in the auroral line intensity (consistent with other studies, see J. Kennicutt et al. 2003). This is because recombination scales with increasing O^{2+} abundance in the ISM, but all LBT Y_p Project targets have low total O abundance by selection. The correction to the [O II] auroral line inten-

sity often produces statistically similar $T_e[\text{O II}]$, although the change in T_e can be significant: the maximum predicted reduction in the [O II] auroral line intensity is 7% in the galaxy J1323-0132, which reduces $T_e[\text{O II}]$ by ~ 3000 K. Accounting for dielectronic recombination in the full sample, 11 nebulae remain 2σ above the D. R. Garnett (1992) T_e scaling relation.

While accounting for dielectronic recombination can lower $T_e[\text{O II}]$, it cannot explain the overall scatter in $T_e[\text{O II}]$ observed in the full sample. Furthermore, no recombination contribution to the [S II] $\lambda 4069,76$ auroral lines has been reported, such that recombination cannot contribute to the scatter in $T_e[\text{S II}]$ plotted in the right panel of Figure 8. The [S II] auroral-to-nebular line ratios in a handful of nebulae indicate T_e in excess of 25 kK, far greater than $T_e[\text{O III}]$ or any other available temperature diagnostic. Given the large wavelength separation between the auroral and nebular lines, both $T_e[\text{O II}]$ and $T_e[\text{S II}]$ are sensitive to errors in the reddening correction. However, systematic uncertainties in $E(B-V)$ work in the opposite direction for the two temperatures, such that biases in $E(B-V)$ cannot explain the trend to high $T_e[\text{S II}]$ and $T_e[\text{O II}]$.

In their work on the DESIRED sample, J. E. Méndez-Delgado et al. (2023b) discuss the possibility of n_e inhomogeneities biasing the auroral-to-nebular line ratios of [O II] and [S II]. The critical densities of the ^2D levels of the O^+ and S^+ ions (on the order of 10^3 cm $^{-3}$ at $T_e = 1.5 \times 10^4$ K) are relatively small for optical CELs. If the ISM shows large n_e variations, then collisional de-excitation of the nebular [O II] and [S II] lines could result in larger auroral-to-nebular line ratios and T_e that are biased higher than predicted for the low-ionization zone. As described in §3.2 and plotted in Figure

6, the auroral-to-nebular line ratios of [O II] and [S II] imply marginally higher average n_e than the nebular line ratios, assuming a characteristic low-ionization zone T_e . The scatter to high T_e [O II] and T_e [S II] in Figure 8 could be influenced by a combination of dielectronic recombination, reddening uncertainties, n_e variations, or other factors not discussed here, such as shock excitation of the [S II] lines or large T_e variations in the low-ionization zone. Given the complexities associated with T_e [O II] and T_e [S II], we recommend avoiding these temperatures for use in measuring chemical abundances in the ISM when other T_e are available, in line with the recommendation of other recent works (D. A. Berg et al. 2020; J. E. Méndez-Delgado et al. 2023b).

5. GAS-PHASE OXYGEN ABUNDANCES

5.1. Ionic Abundance Calculations

With T_e and n_e , we can now directly measure metal ionic abundances in the ISM of each LBT Y_p Project target. In this work, we focus on the total abundance of O in the ISM, which is required to assess the relation between He/H and O/H and constrain Y_p . In Paper VI, we will derive the chemical abundance patterns of many elements (from He to Fe) in a large sample of metal-poor nebulae.

To determine the ionic abundance of O⁺ and O²⁺ in the ISM, we select the T_e measured in the MODS data that is most representative for the ionization zone of interest. For the high-ionization zone, we adopt the directly-measured T_e [O III], which is available for all targets in the sample. For the low-ionization zone, we use T_e [N II] when available. O. A. Kurichin et al. (2021a) argue that a direct T_e [O II] is required to reliably measure the abundance of O⁺/H⁺ and its uncertainty, which can change significantly if a T_e scaling relation is adopted. Indeed, T_e scaling relations may not capture the simultaneous T_e trends in the low-metallicity ISM, such as the B. E. J. Pagel et al. (1992) relation in Figure 8. However, T_e [O II] shows large dispersion around the T_e scaling relations and can be biased by dielectronic recombination and density fluctuations in the ISM, as discussed in §4.2. These effects may introduce spurious trends in He/H vs. O/H and other relative abundance patterns, so we use the T_e [O III] and the photoionization model scaling relation of D. R. Garnett (1992) to infer the low-ionization zone temperature when T_e [N II] is unavailable. We propagate an additional 610 K into the inferred temperature uncertainty, which accounts for the scatter observed in empirical T_e [N II] and T_e [O III] data (N. S. J. Rogers et al. 2021) and mitigates the low uncertainties on O⁺/H⁺ discussed in O. A. Kurichin et al. (2021a). This may be an underestimate of the true dispersion in empirical T_e in the low-metallicity nebulae, but we do not have the data to better constrain the dispersion or scaling relation for T_e [N II]- T_e [O III]. Adopting T_e [O II] for the low-ionization zone T_e can change the resulting 12+log(O/H) in

individual objects, but does not alter the number of very low-metallicity galaxies that are critical for constraining Y_p via a weighted average (see Paper IV).

Finally, we utilize the direct T_e [S III] for the intermediate-ionization zone, or apply Equation 3 to infer the intermediate-ionization zone T_e when [S III] λ 6312 is not detected. Similar to the low-ionization zone, we consider σ_{int} when inferring the intermediate-ionization zone temperature (in the same manner as N. S. J. Rogers et al. 2021). The intermediate-ionization zone T_e is not used for deriving O⁺ and O²⁺, but is necessary for future analysis of the S²⁺, Ar²⁺, and Cl²⁺ abundances in the LBT Y_p Project nebulae.

To measure ionic abundances relative to H⁺, we apply the PYNEB GETIONABUNDANCE function using the emission line intensity ratio relative to H β , the measured or inferred ionization zone T_e , and the adopted n_e from §3.1. We calculate the uncertainty in the measured ionic abundance using the line intensity ratio uncertainty and the error on T_e . The ionic and total abundances of O calculated for the full sample are provided in Table 3.

In general, it is not possible to detect emission from all relevant ionization states of a given element in the ISM. Correcting for unobserved ionization states, either through arguments of similar IP (M. Peimbert & R. Costero 1969; K. V. Croxall et al. 2016) or through photoionization model predictions (T. X. Thuan et al. 1995; Y. I. Izotov et al. 2006b; G. Delgado-Ingala et al. 2014; A. Amayo et al. 2021), represents a large systematic uncertainty present in most chemical abundance studies. Fortunately, O is the only element with all relevant ionization states easily detectable within the MODS optical/NIR spectra. We assume that the total O abundance is O/H = O⁺/H⁺ + O²⁺/H⁺, implying negligible contributions from neutral O or any higher ionization states. While [O I] emission lines are clearly detected in the MODS spectra (see Figure 3), this emission may not be cospatial with the ionized gas emitting the H I recombination lines or where we have a direct T_e measurement. Therefore, the inclusion of O⁰/H⁺ in the total O abundance is inappropriate for the present study. The ionization conditions of the LBT Y_p Project sample are relatively high, with large O₃₂ and significant detections of narrow, nebular He II λ 4686, as well as other high-ionization emission lines such as [Ar IV] λ 4741,40 and [Fe V] λ 4227. It is natural to expect an amount of O³⁺ in the ISM given these ionization conditions, but the detection of O IV emission lines is only possible with UV or MIR spectroscopy. In rare instances where O IV lines have been detected in extreme star-forming galaxies, the resulting ionic abundance of O³⁺/H⁺ in the ISM is only \lesssim 2% of the global O abundance (D. A. Berg et al. 2021; R. J. Rickards Vaught et al. 2025). Such a contribution is less than the typical uncertainties on O/H measured in this sample, so we do not attempt to account for the O³⁺ ions

when reporting the total O/H. In addition to the emission line intensities and T_e [O III], the O/H abundance of each nebulae is provided for the final calibration of Y vs. O/H to infer Y_p (see Paper IV).

5.2. O/H and Literature Comparison

The galaxies presented in this work were originally selected for their low gas-phase O/H, which is required to assess the relative abundance of He/H in gas of near primordial composition. A handful of moderately metal-enriched galaxies were included in the sample to explore the increase in He/H with O/H, a trend expected based on stellar nucleosynthesis and chemical evolution models (e.g., [M. K. Weller et al. 2025](#)). To measure He/H also requires many faint He I recombination lines, some of which are fainter than the auroral lines necessary to directly measure T_e and O/H. As such, fainter, potentially extremely metal-poor objects where He I lines were unlikely to be robustly detected were deprioritized in initial target selection. Given these selection criteria, it is unsurprising that we find the majority of the LBT Y_p Project nebulae are metal poor, with $12+\log(O/H) < 20\%$ the solar O abundance. Specifically, the oxygen abundances measured from the LBT/MODS spectra span $12+\log(O/H) = [7.00, 8.30]$ dex with median uncertainty of 4%. The low uncertainty reflects the target selection and the quality of optical/NIR data accessible with LBT/MODS.

As a consequence of this methodology, we do not report many new metal-poor galaxies as part of this analysis. The exception is J0807+3414, which was selected based on its inferred metallicity of $12+\log(O/H) = 7.69 \pm 0.09$ dex from [J. Sánchez Almeida et al. \(2016\)](#). The direct-method metallicity measured in J0807+3414 is $12+\log(O/H) = 7.686 \pm 0.014$ dex, in excellent agreement with the indirect estimate but with significantly lower uncertainty. For the remaining 61 galaxies, it is worthwhile to compare the direct O/H reported here to those from previous literature analyses that were considered when finalizing the target selection. In Figure 9, we plot the total O/H abundance measured as part of the LBT Y_p Project on the horizontal axis. We define $\delta(O/H)$ as the difference between the $12+\log(O/H)$ measured in this work and the reported $12+\log(O/H)$ of the same nebula from various literature sources. We color code each point based on the source of the previous O/H measurement, where the literature sources with multiple nebulae observed in the LBT Y_p Project include: [Y. I. Izotov & T. X. Thuan \(2007, red\)](#), [Y. I. Izotov et al. \(2007, orange\)](#), [Y. I. Izotov et al. \(2012, yellow\)](#), [Y. I. Izotov et al. \(2014, dark green\)](#), [V. Fernández et al. \(2018, light green\)](#), [T. Hsyu et al. \(2020, blue\)](#), [T. Kojima et al. \(2020, pink\)](#), [Y. I. Izotov et al. \(2021, purple\)](#), [O. A. Kurichin et al. \(2021b, black\)](#), and [A. Matsumoto et al. \(2022, white\)](#). The gray points represent a compilation of literature sources with a single galaxy in common with the

LBT Y_p Project (including [Y. I. Izotov et al. 1999, 2006a](#); [E. D. Skillman et al. 2013](#); [T. Hsyu et al. 2018](#); [F. Annibali et al. 2019](#); [E. Aver et al. 2022](#); [K. Nakajima et al. 2022](#); [K. Watanabe et al. 2024](#)).

We find good consistency between the presented abundances and those in the literature, where the average $\delta(O/H)$ is just -0.006 dex. However, it is notable that the standard deviation in $\delta(O/H)$ is 0.095 dex, larger than the uncertainty on most $12+\log(O/H)$ reported in the LBT Y_p Project nebulae. Numerous factors can contribute to the difference in O/H, some of which are obvious in the largest outliers of Figure 9. For example, the galaxy UM420 has a metallicity of $12+\log(O/H) = 8.30 \pm 0.10$ dex, the highest measured in the LBT Y_p Project sample. The metallicity for UM420 reported in [Y. I. Izotov et al. \(2007\)](#) and [T. Hsyu et al. \(2020\)](#) is ~ 8.0 dex, hence the selection for observation as part of the LBT Y_p Project. The ~ 0.3 dex difference in O/H is related to the morphology of UM420. From integral field spectroscopy, [B. L. James et al. \(2010\)](#) found that the two star-forming regions in UM420 have direct $12+\log(O/H) \approx 8.25 \pm 0.07$ dex, in good agreement with the LBT Y_p Project measurement. However, the integrated emission in UM420 results in $12+\log(O/H) = 8.03^{+0.17}_{-0.13}$ dex, consistent with the measurements from [Y. I. Izotov et al. \(2007\)](#) and [T. Hsyu et al. \(2020\)](#). As illustrated in this example, differences in the aperture size and placement can incorporate different components of the ISM, resulting in differences in the integrated optical spectrum, measured physical conditions, and final $12+\log(O/H)$ reported for individual galaxies.

Differences in methodology will also introduce offsets in the reported $12+\log(O/H)$. Consider the galaxy HS0122+0743, which has $12+\log(O/H) = 7.580 \pm 0.015$ dex as measured from the MODS spectrum. This metallicity is similar to that obtained from [Y. I. Izotov et al. \(2007\)](#), [T. Hsyu et al. \(2020\)](#), and [K. Nakajima et al. \(2022\)](#), but it 0.33 dex lower than $12+\log(O/H)$ reported in [V. Fernández et al. \(2018\)](#). The T_e [O III] reported in the latter is in good agreement with the T_e [O III] measured from the MODS spectrum, but [V. Fernández et al. \(2018\)](#) adopted T_e [S III], with the use of a T_e scaling relation, for O²⁺ ionic abundances on account of the lower temperature uncertainty. This produces a significantly different high-ionization zone T_e that manifests as the large $\delta(O/H)$ in this galaxy. Furthermore, direct measurements of T_e [N II] from the MODS spectra are possible in a portion of the LBT Y_p Project sample (see Figure 8), and these T_e [N II] are prioritized for the low-ionization zone T_e and the measurement of O⁺. Although O⁺ is not the dominant ionization state of O, the high T_e [N II] measured in some of the LBT Y_p Project nebulae results in lower total $12+\log(O/H)$ than reported in the literature studies. An extreme example is the T_e structure in HS0837+4717: this galaxy has a direct T_e [N II] = $(1.98 \pm 0.24) \times 10^4$ K, which

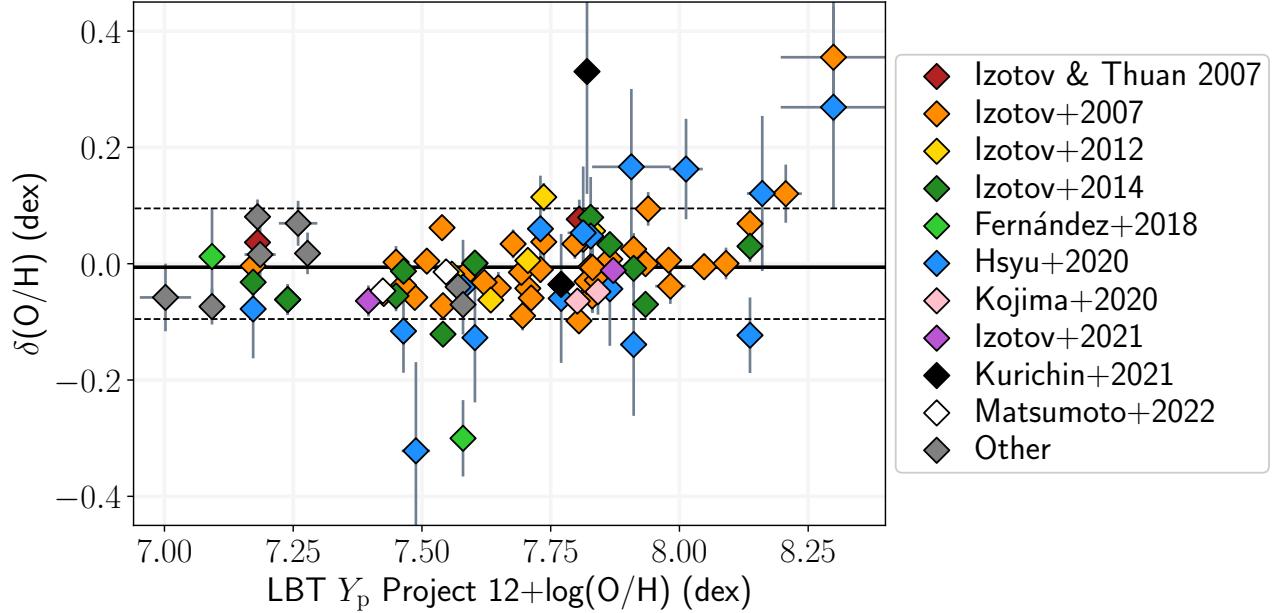


Figure 9. 12+log(O/H) measured from the LBT/MODS spectra of the LBT Y_p Project sample is plotted on the horizontal axis. The vertical axis plots $\delta(O/H)$, or the difference between LBT Y_p Project and literature 12+log(O/H) for the same galaxy (color-coded by source, see references in main text). The average offset in O/H is plotted as a solid black line, while the dashed lines represent the standard deviation in $\delta(O/H)$ for all literature abundances. While the scatter in $\delta(O/H)$ is larger than the typical error on O/H, and there are galaxies that show large variations in O/H, the measurement of 12+log(O/H) is generally consistent across observations, where the average $\delta(O/H)$ is -0.006 dex.

is over 3000 K higher than predicted from the D. R. Garnett (1992) T_e scaling relation and the direct T_e [O III]. It is no surprise, then, that HS0837+4717 shows $\delta(O/H) \approx -0.12$ dex when compared to the direct measurement presented in Y. I. Izotov et al. (2014). To a lesser extent, a change to the adopted density could also contribute to a change in the O⁺ ionic abundance and $\delta(O/H)$, although most of the LBT Y_p Project targets are close to the low-density limit (Figure 5).

Numerous other factors could produce variations in 12+log(O/H) reported here and in the literature. Some of these include differences in the adopted atomic data (D. A. Berg et al. 2015; C. Morisset et al. 2020), the use of the [O II] auroral lines for O⁺ abundances (M. Rodríguez 2020), and corrections due to the contamination of [O III] $\lambda 4363$ from [Fe II] emission (M. Curti et al. 2017; N. S. J. Rogers et al. 2022, although this is generally a small correction, see §2.2). In summary, although individual measurements of 12+log(O/H) in a given galaxy can vary significantly, the metallicity measured from the LBT/MODS spectroscopy and reported in the literature are generally consistent and indicate that the sample is metal-poor in nature. The utility of the LBT Y_p Project sample is in its homogeneity, where the 62 galaxies have been observed with the same instruments and analyzed self-consistently to produce a dataset capable of robustly constraining the primordial He abundance.

6. CONCLUSIONS

In this paper, we describe the LBT/MODS observations of the galaxies observed as part of the LBT Y_p Project. These galaxies have been selected for observation based on their low gas-phase metallicities and large H I EWs. The large, homogeneous sample provides an opportunity to measure the physical conditions in the low-metallicity ISM of local star-forming galaxies. Our key findings are:

1. We find that the emission lines in the average MODS spectrum are not described by Gaussian profiles, a result of the telescope optics. We implement a new emission line fitting methodology, employing super-Gaussian emission line profiles that better capture the position, amplitude, and shape of the emission lines measured in MODS (Equations 1 and 2). Furthermore, we fit two broad Gaussian profiles to the H β , [O III] $\lambda 4959, 5007$, and H α emission lines in a majority of the LBT Y_p Project galaxies (Figure 2). These more complex line profiles are crucial for faint emission lines neighboring bright features (e.g., He I $\lambda 5015$ and [N II] $\lambda 6548, 84$), where the flux of the faint lines may be biased too high if the broad wings are included in the narrow line flux. Finally, we preserve the native resolution of MODS, allowing for a simultaneous measurement of [O II] $\lambda 3726, 29$ and n_e [O II].

2. The ionization conditions, as traced by various emission line ratios, in the LBT Y_p Project nebulae are very high. The positions of the galaxies in the traditional BPT diagrams are consistent with very low gas-phase O/H (Figure 3), while the relative metal line ratios are similar to those measured in high- z extreme emission line galaxies (Figure 4). There are 50 galaxies with significant, narrow, nebular He II $\lambda 4686$ emission, ranging from 0.2 to 3.4% the intensity of H β . A subset of galaxies also show the very high-ionization emission from [Fe V] $\lambda 4227$. Such highly ionized gas is challenging to produce from stars alone, and may hint at more complicated physics in the ISM.
3. We derive the physical conditions, T_e and n_e , in the ISM of the LBT Y_p Project targets. This is an important step for the measurement of Y_p : T_e [O III] acts as a weak prior on T_e (He I), and both T_e and n_e are required to measure the gas-phase abundance of O $^+$ and O $^{2+}$. The simultaneous n_e [S II] and n_e [O II] generally agree, although the marginally lower average n_e [S II] could be related to DIG contamination of the [S II] strong lines. Both n_e [S II] and n_e [O II] are significantly lower than the densities measured from the [Cl III] and [Ar IV] emission lines (Figure 5). This offset persists when using the [O II] and [S II] auroral-to-nebular line ratios as density tracers, which do predict generally larger n_e [O II] than the nebular lines alone (Figure 6). However, the use of the densities from higher ionization ions such as Ar $^{3+}$ does not significantly affect T_e [O III] or O $^{2+}$ abundances.
4. The high-quality MODS spectra resolve the T_e structure in the multi-phase ISM, and we find a strong correlation between T_e [S III] and T_e [O III] from 60 nebulae (Figure 7). The resulting T_e scaling relations (Equations 3 and 4) can be used to infer the temperature of the intermediate- and high-ionization zones when a direct T_e is unavailable in the metal-poor, high-ionization ISM. The small scatter about this relation is in contrast to the T_e [S III] and T_e [O III] trends of more metal-rich H II regions. Combinations with larger T_e samples in metal-rich nebulae will assess the shape of these relations and the drivers of scatter in T_e [S III] and T_e [O III].
5. T_e [N II] is measured in fewer galaxies, a result of the low metallicities and high ionization conditions in the present sample. Nevertheless, we find that the direct T_e [O III]- T_e [N II] tend to scatter around the T_e scaling relations of D. R. Garnett (1992) and N. S. J. Rogers et al. (2021). However, there are a handful of LBT Y_p Project targets with very high T_e [N II] $\gtrsim 2 \times 10^4$ K, which are not predicted by empirical or photoionization model T_e scaling relations. Furthermore, multiple

galaxies show elevated T_e [O II] and T_e [S II] relative to T_e [O III] (Figure 8), a trend that could be related to the density sensitivity of the [O II] and [S II] nebular lines or other mechanisms of producing the auroral lines of these ionic species. Given these systematic uncertainties and the large observed scatter in T_e , we caution against the use of T_e [O II] and T_e [S II] for ionic abundance measurements when other T_e are available.

6. With the T_e , n_e , and the collisionally excited metal lines available in the optical, we measure the total O abundance in the ISM of the LBT Y_p Project galaxies. Given the high-fidelity constraints on T_e [O III], the average uncertainty on the O/H is just 4%. We compare the direct O/H in individual objects to measurements from various literature sources, finding an average offset of δ (O/H) = -0.006 dex with a standard deviation of 0.095 dex (Figure 9). While 12+log(O/H) can vary significantly for some objects (as discussed in §5.2), the O/H measurements are, on average, consistent across observations.

The data presented in this manuscript provide the optical H I and He I emission lines fluxes and T_e [O III] required to determine the ISM He/H abundance, measure the He/H-O/H relation, and constrain Y_p , as will be detailed in Paper IV of this series. The LBT/MODS spectra of the LBT Y_p Project galaxies reveal the presence of emission lines from many other elements in the ISM. In Paper VI of this series, we will use the physical conditions derived in this analysis to examine the chemical abundance patterns, from He to Fe, in the low-metallicity ISM. Such a sample will provide a necessary comparison sample for low-metallicity galaxies being observed with JWST. Furthermore, we will determine if the peculiar emission line ratios or physical conditions, such as T_e [N II] $>$ T_e [O III], are indicators of anomalous gas-phase abundance patterns.

ACKNOWLEDGEMENTS

This work was supported by funds provided by NSF Collaborative Research Grants AST-2205817 to RWP, AST-2205864 to EDS, and AST-2205958 to EA. Our team workshop at OSU in July 2024 was sponsored in part by OSU's Center for Cosmology and AstroParticle Physics (CCAPP).

This work is based on observations made with the Large Binocular Telescope. The LBT is an international collaboration among institutions in the United States, Italy and Germany. LBT Corporation Members are: The University of Arizona on behalf of the Arizona Board of Regents; Istituto Nazionale di Astrofisica, Italy; LBT Beteiligungsgesellschaft, Germany, representing the Max-Planck Society,

The Leibniz Institute for Astrophysics Potsdam, and Heidelberg University; The Ohio State University, and The Research Corporation, on behalf of The University of Notre Dame, University of Minnesota and University of Virginia. Observations have benefited from the use of ALTA Center (alta.arcetri.inaf.it) forecasts performed with the Astro-Meso-Nh model. Initialization data of the ALTA automatic forecast system come from the General Circulation Model (HRES) of the European Centre for Medium Range Weather Forecasts.

This research used the facilities of the Italian Center for Astronomical Archive (IA2) operated by INAF at the Astronomical Observatory of Trieste.

EDS, EA, DAB, NSJR, and JHM would like to acknowledge and thank Stanley Hubbard for his generous gift to the

University of Minnesota that allowed the University to become a member of the LBT collaboration.

Facilities: LBT (MODS), LBT (LUCI)

Software: `astropy` ([Astropy Collaboration et al. 2013, 2018, 2022](#)), `jupyter` ([T. Kluyver et al. 2016](#)), `modSIDL` ([K. V. Croxall & R. W. Pogge 2019](#)), `modSCCDRed` ([R. Pogge 2019](#)), `PypeIt` ([J. X. Prochaska et al. 2020; J. X. Prochaska et al. 2020](#)) `PyNeb` ([V. Luridiana et al. 2012, 2015](#)), `numpy` ([C. R. Harris et al. 2020](#)), `scipy` ([P. Virtanen et al. 2020](#))

APPENDIX

A. MEASURED PROPERTIES

In this appendix, we provide tables with the measured properties in the LBT Y_p Project sample. We summarize the H and He recombination line fluxes measured from the MODS spectra in Table 2, and we report the direct n_e , T_e , ionic and total abundances of O in Table 3.

Table 2. LBT Y_p Project Line Flux Ratios and EWs

Line	AGC198691	DDO68	HS0029+1748	HS0122+0743	HS0134+3415	HS0811+4913	HS0837+4717
H12 $\lambda 3750$	0.0108 \pm 0.0071	0.0246 \pm 0.0035	0.0203 \pm 0.0016	0.0236 \pm 0.0011	0.0247 \pm 0.0005	0.0227 \pm 0.0013	0.0246 \pm 0.0018
EW	0.56	1.50	2.65	4.05	5.70	6.52	3.17
H11 $\lambda 3771$	0.0167 \pm 0.0073	0.0293 \pm 0.0034	0.0259 \pm 0.0018	0.0301 \pm 0.0017	0.0320 \pm 0.0007	0.0291 \pm 0.0011	0.0304 \pm 0.0015
EW	0.85	1.81	3.38	5.14	7.43	8.48	3.92
H10 $\lambda 3797$	0.0228 \pm 0.0068	0.0423 \pm 0.0036	0.0355 \pm 0.0018	0.0405 \pm 0.0017	0.0436 \pm 0.0008	0.0409 \pm 0.0010	0.0418 \pm 0.0014
EW	1.15	2.64	4.60	6.89	10.17	12.14	5.41
H9 $\lambda 3835$	0.0434 \pm 0.0062	0.0580 \pm 0.0032	0.0495 \pm 0.0016	0.0554 \pm 0.0013	0.0617 \pm 0.0010	0.0564 \pm 0.0011	0.0573 \pm 0.0014
EW	2.16	3.69	6.38	9.35	14.54	17.22	7.41
He I+H8 $\lambda 3889$	0.1516 \pm 0.0049	0.1950 \pm 0.0046	0.1542 \pm 0.0024	0.1648 \pm 0.0023	0.1678 \pm 0.0024	0.1600 \pm 0.0024	0.1521 \pm 0.0025
EW	7.60	12.38	20.34	28.85	40.46	50.37	20.49
He I $\lambda 4026$	0.0134 \pm 0.0043	0.0107 \pm 0.0025	0.0145 \pm 0.0009	0.0148 \pm 0.0007	0.0158 \pm 0.0004	0.0145 \pm 0.0004	0.0150 \pm 0.0008
EW	0.76	0.75	1.93	2.74	3.96	4.84	2.17
H δ $\lambda 4101$	0.2232 \pm 0.0059	0.2556 \pm 0.0048	0.2146 \pm 0.0033	0.2259 \pm 0.0034	0.2329 \pm 0.0036	0.2223 \pm 0.0035	0.2309 \pm 0.0035
EW	12.35	18.43	29.22	43.15	61.14	75.35	34.56
H γ $\lambda 4340$	0.4485 \pm 0.0083	0.4669 \pm 0.0077	0.4161 \pm 0.0062	0.4308 \pm 0.0064	0.4401 \pm 0.0068	0.4149 \pm 0.0064	0.4308 \pm 0.0066
EW	28.34	40.89	63.62	92.14	129.91	159.01	74.17
He I $\lambda 4388$...	0.0025 \pm 0.0022	0.0040 \pm 0.0006	0.0041 \pm 0.0009	0.0042 \pm 0.0003	0.0040 \pm 0.0004	0.0038 \pm 0.0013
EW	...	0.23	0.61	0.89	1.26	1.55	0.67
He I $\lambda 4471$	0.0307 \pm 0.0041	0.0324 \pm 0.0027	0.0350 \pm 0.0008	0.0348 \pm 0.0010	0.0367 \pm 0.0006	0.0347 \pm 0.0006	0.0388 \pm 0.0014
EW	2.04	3.11	5.53	7.88	11.49	14.20	7.16
He II $\lambda 4686$...	0.0274 \pm 0.0019	0.0087 \pm 0.0005	0.0097 \pm 0.0006	0.0058 \pm 0.0003	0.0019 \pm 0.0004	0.0190 \pm 0.0009
EW	...	3.04	0.24	2.39	1.97	0.83	3.85

Table 2 *continued*

Table 2 (continued)

Line	AGC198691	DDO68	HS0029+1748	HS0122+0743	HS0134+3415	HS0811+4913	HS0837+4717
He I $\lambda 4922$	0.0060 \pm 0.0037	0.0082 \pm 0.0020	0.0103 \pm 0.0006	0.0103 \pm 0.0006	0.0100 \pm 0.0004	0.0095 \pm 0.0003	0.0121 \pm 0.0019
EW	0.47	1.05	1.88	2.82	3.73	4.62	2.74
He I $\lambda 5016$	0.0216 \pm 0.0037	0.0192 \pm 0.0021	0.0203 \pm 0.0007	0.0204 \pm 0.0007	0.0173 \pm 0.0005	0.0191 \pm 0.0004	0.0255 \pm 0.0019
EW	1.78	2.60	3.80	5.82	6.76	9.69	6.03
He I $\lambda 5876$	0.1106 \pm 0.0042	0.0952 \pm 0.0022	0.1181 \pm 0.0024	0.1179 \pm 0.0019	0.1106 \pm 0.0018	0.1336 \pm 0.0021	0.1423 \pm 0.0022
EW	12.48	22.37	29.79	45.85	59.01	88.90	45.98
H α $\lambda 6563$	3.0802 \pm 0.0477	2.9633 \pm 0.0471	3.3047 \pm 0.0491	3.3497 \pm 0.0496	3.1314 \pm 0.0492	3.7694 \pm 0.0590	3.8129 \pm 0.0581
EW	442.89	917.92	956.89	1492.35	1940.75	2841.61	1433.58
He I $\lambda 6678$	0.0344 \pm 0.0022	0.0272 \pm 0.0007	0.0357 \pm 0.0006	0.0355 \pm 0.0007	0.0324 \pm 0.0005	0.0416 \pm 0.0007	0.0380 \pm 0.0007
EW	5.18	8.78	10.45	16.17	20.32	31.29	14.60
He I $\lambda 7065$	0.0257 \pm 0.0046	0.0238 \pm 0.0013	0.0295 \pm 0.0005	0.0430 \pm 0.0008	0.0329 \pm 0.0005	0.0431 \pm 0.0007	0.0879 \pm 0.0015
EW	4.08	8.82	9.54	22.44	23.55	36.26	39.47
He I $\lambda 7281$	0.0036 \pm 0.0046	0.0055 \pm 0.0011	0.0063 \pm 0.0007	0.0085 \pm 0.0007	0.0069 \pm 0.0002	0.0089 \pm 0.0003	0.0074 \pm 0.0067
EW	0.62	2.22	2.13	4.63	5.13	7.92	3.38
P15 $\lambda 8545$...	0.0058 \pm 0.0010	0.0054 \pm 0.0006	0.0055 \pm 0.0007	0.0064 \pm 0.0003	0.0092 \pm 0.0003	0.0070 \pm 0.0016
EW	...	4.04	2.70	4.62	7.99	17.62	5.31
P14 $\lambda 8598$...	0.0081 \pm 0.0011	0.0078 \pm 0.0008	0.0080 \pm 0.0007	0.0082 \pm 0.0002	0.0112 \pm 0.0004	0.0109 \pm 0.0013
EW	...	5.91	3.92	6.89	10.50	21.79	8.33
P13 $\lambda 8665$	0.0268 \pm 0.0111	0.0094 \pm 0.0012	0.0098 \pm 0.0010	0.0109 \pm 0.0006	0.0097 \pm 0.0003	0.0140 \pm 0.0004	0.0122 \pm 0.0008
EW	6.32	7.17	4.95	9.55	12.63	27.98	9.53
P12 $\lambda 8750$...	0.0096 \pm 0.0045	0.0138 \pm 0.0010	0.0136 \pm 0.0008	0.0131 \pm 0.0004	0.0183 \pm 0.0025	0.0143 \pm 0.0006
EW	...	7.76	7.06	12.27	17.52	37.73	11.49
P11 $\lambda 8863$	0.0158 \pm 0.0104	0.0152 \pm 0.0057	0.0171 \pm 0.0008	0.0175 \pm 0.0010	0.0168 \pm 0.0005	0.0232 \pm 0.0032	0.0201 \pm 0.0007
EW	4.19	13.36	8.93	16.31	23.15	49.84	16.62
P10 $\lambda 9015$	0.0233 \pm 0.0039	0.0199 \pm 0.0019	0.0217 \pm 0.0006	0.0272 \pm 0.0006	0.0219 \pm 0.0006	0.0298 \pm 0.0008	0.0248 \pm 0.0012
EW	6.65	16.38	11.27	24.93	29.55	57.23	18.07
P9 $\lambda 9229$	0.0215 \pm 0.0041	0.0284 \pm 0.0015	0.0294 \pm 0.0023	0.0262 \pm 0.0039	0.0308 \pm 0.0013	0.0423 \pm 0.0013	0.0372 \pm 0.0026
EW	6.51	25.77	16.65	26.88	46.43	92.28	30.14
P8 $\lambda 9546$	0.0430 \pm 0.0186	0.0368 \pm 0.0057	0.0539 \pm 0.0019	0.0527 \pm 0.0018	0.0419 \pm 0.0020	0.0623 \pm 0.0025	0.0458 \pm 0.0025
EW	12.40	41.24	32.48	54.63	67.41	143.15	39.14
z	0.00171	0.00168	0.00707	0.00976	0.01949	0.00185	0.04197
$F_{H\beta}$	9.5 \pm 0.1	25.3 \pm 0.3	141.6 \pm 1.5	114.0 \pm 1.2	202.4 \pm 2.2	142.3 \pm 1.6	159.9 \pm 1.7
$EW_{H\beta}$	76.88	122.19	179.42	266.04	365.41	472.55	219.50
$E(B-V)$	0.10 \pm 0.01	0.06 \pm 0.01	0.15 \pm 0.01	0.19 \pm 0.01	0.12 \pm 0.01	0.27 \pm 0.01	0.26 \pm 0.01
a_H	1.4 $^{+0.4}_{-0.4}$	0.0 $^{+0.4}_{-0.0}$	3.5 $^{+0.5}_{-0.5}$	0.3 $^{+0.8}_{-0.3}$	2.8 $^{+1.2}_{-1.2}$	0.0 $^{+1.4}_{-0.0}$	0.0 $^{+0.6}_{-0.0}$

NOTE—Emission line fluxes required to measure He/H. Each row corresponds to the observed flux of a H I, He I, or He II recombination line relative to the observed flux of H β (top) and that line's EW (in Å, bottom). The last five rows provide the spectroscopic z , observed flux of H β (in 10^{-16} erg/s/cm 2), the EW of H β (in Å), $E(B-V)$ and Balmer absorption EW, a_H , inferred from the methods of §2.3. Table truncated at seven targets, the complete version is available in machine readable format.

Table 3. LBT Y_p Project Physical Conditions and Oxygen Abundances

Property	AGC198691	DDO68	HS0029+1748	HS0122+0743	HS0134+3415	HS0811+4913	HS0837+4717
$n_e[\text{S II}] (\text{cm}^{-3})$	35^{+570}_{-20}	55^{+62}_{-29}	56^{+13}_{-12}	95^{+18}_{-16}	83^{+27}_{-25}	91^{+13}_{-13}	431^{+38}_{-36}
$n_e[\text{O II}] (\text{cm}^{-3})$	21^{+94}_{-12}	9^{+50}_{-5}	33^{+13}_{-12}	55^{+15}_{-15}	104^{+16}_{-15}	151^{+18}_{-16}	546^{+46}_{-41}
$n_e[\text{Cl III}] (\text{cm}^{-3})$	2205^{+12760}_{-1270}
$n_e[\text{Ar IV}] (\text{cm}^{-3})$	680^{+1176}_{-391}	...	172^{+160}_{-91}	851^{+407}_{-348}	1913^{+1298}_{-840}
$n_{e,Used} (\text{cm}^{-3})$	100^{+50}_{-50}	100^{+50}_{-50}	100^{+50}_{-50}	100^{+50}_{-50}	100^{+50}_{-50}	100^{+50}_{-50}	488^{+30}_{-27}
$T_e[\text{N II}] (\text{K})$	13200 ± 1700	12600 ± 700	19800 ± 2400
$T_e[\text{O II}] (\text{K})$...	13000 ± 3400	15400 ± 400	15600 ± 500	16200 ± 500	12900 ± 300	...
$T_e[\text{S II}] (\text{K})$	19200 ± 2700	15800 ± 1200	15400 ± 1100	...
$T_e[\text{S III}] (\text{K})$...	17000 ± 1600	12400 ± 200	16100 ± 400	15500 ± 300	13900 ± 200	18400 ± 900
$T_e[\text{Ar III}] (\text{K})$	14900 ± 2600
$T_e[\text{O III}] (\text{K})$	20000 ± 1300	18900 ± 500	12900 ± 100	17800 ± 200	16300 ± 200	14600 ± 200	19500 ± 300
$T_{e,Low} (\text{K})$	17000 ± 1100	16200 ± 700	12000 ± 600	15500 ± 600	13200 ± 1700	12600 ± 700	19800 ± 2400
$T_{e,Int} (\text{K})$	18500 ± 1200	17000 ± 1600	12400 ± 200	16100 ± 400	15500 ± 300	13900 ± 200	18400 ± 900
$T_{e,High} (\text{K})$	20000 ± 1300	18900 ± 500	12900 ± 100	17800 ± 200	16300 ± 200	14600 ± 200	19500 ± 300
$O^+/\text{H}^+ (\times 10^5)$	0.24 ± 0.05	0.27 ± 0.03	1.43 ± 0.28	0.53 ± 0.07	0.51 ± 0.25	1.54 ± 0.33	0.21 ± 0.07
$O^{2+}/\text{H}^+ (\times 10^5)$	0.77 ± 0.11	1.25 ± 0.07	9.74 ± 0.32	3.27 ± 0.11	6.42 ± 0.19	7.98 ± 0.25	3.26 ± 0.12
$12+\log(\text{O/H})$	7.002 ± 0.050	7.181 ± 0.022	8.048 ± 0.016	7.580 ± 0.015	7.841 ± 0.020	7.979 ± 0.019	7.541 ± 0.017

NOTE—Physical conditions, ionic and total O abundances measured in the Y_p Project nebulae. Each row corresponds to a property measured in a given target (columns). These properties are: Direct n_e measurements (Rows 1-4), adopted n_e in the ISM (5, described in §3.2), direct T_e (6-11), adopted T_e for each ionization zone (12-14), ionic abundances of O^+ and O^{2+} (15-16), and the total O abundance, $12+\log(\text{O/H})$ (17). Table truncated at seven targets, the complete version is available in machine readable format.

REFERENCES

Amayo, A., Delgado-Ingla, G., & Stasińska, G. 2021, MNRAS, 505, 2361, doi: [10.1093/mnras/stab1467](https://doi.org/10.1093/mnras/stab1467)

Andrews, B. H., & Martini, P. 2013, ApJ, 765, 140, doi: [10.1088/0004-637X/765/2/140](https://doi.org/10.1088/0004-637X/765/2/140)

Annibali, F., La Torre, V., Tosi, M., et al. 2019, MNRAS, 482, 3892, doi: [10.1093/mnras/sty2911](https://doi.org/10.1093/mnras/sty2911)

Aravindan, A., Canalizo, G., Secret, N., Satyapal, S., & Bohn, T. 2024, ApJ, 975, 60, doi: [10.3847/1538-4357/ad702b](https://doi.org/10.3847/1538-4357/ad702b)

Arellano-Córdova, K. Z., & Rodríguez, M. 2020, MNRAS, 497, 672, doi: [10.1093/mnras/staa1759](https://doi.org/10.1093/mnras/staa1759)

Astropy Collaboration, Robitaille, T. P., Tollerud, E. J., et al. 2013, A&A, 558, A33, doi: [10.1051/0004-6361/201322068](https://doi.org/10.1051/0004-6361/201322068)

Astropy Collaboration, Price-Whelan, A. M., Sipőcz, B. M., et al. 2018, AJ, 156, 123, doi: [10.3847/1538-3881/aabc4f](https://doi.org/10.3847/1538-3881/aabc4f)

Astropy Collaboration, Price-Whelan, A. M., Lim, P. L., et al. 2022, ApJ, 935, 167, doi: [10.3847/1538-4357/ac7c74](https://doi.org/10.3847/1538-4357/ac7c74)

Aver, E., Berg, D. A., Hirschauer, A. S., et al. 2022, MNRAS, 510, 373, doi: [10.1093/mnras/stab3226](https://doi.org/10.1093/mnras/stab3226)

Aver, E., Berg, D. A., Olive, K. A., et al. 2021, JCAP, 2021, 027, doi: [10.1088/1475-7516/2021/03/027](https://doi.org/10.1088/1475-7516/2021/03/027)

Aver, E., et al. 2026,

Baldwin, J. A., Phillips, M. M., & Terlevich, R. 1981, PASP, 93, 5, doi: [10.1086/130766](https://doi.org/10.1086/130766)

Bautista, M. A., Fivet, V., Ballance, C., et al. 2015, ApJ, 808, 174, doi: [10.1088/0004-637X/808/2/174](https://doi.org/10.1088/0004-637X/808/2/174)

Bedregal, A. G., Aragón-Salamanca, A., & Merrifield, M. R. 2006, MNRAS, 373, 1125, doi: [10.1111/j.1365-2966.2006.11031.x](https://doi.org/10.1111/j.1365-2966.2006.11031.x)

Beirle, S., Lampel, J., Lerot, C., Sihler, H., & Wagner, T. 2017, Atmospheric Measurement Techniques, 10, 581, doi: [10.5194/amt-10-581-2017](https://doi.org/10.5194/amt-10-581-2017)

Berg, D. A., Chisholm, J., Erb, D. K., et al. 2021, ApJ, 922, 170, doi: [10.3847/1538-4357/ac141b](https://doi.org/10.3847/1538-4357/ac141b)

Berg, D. A., Pogge, R. W., Skillman, E. D., et al. 2020, ApJ, 893, 96, doi: [10.3847/1538-4357/ab7eab](https://doi.org/10.3847/1538-4357/ab7eab)

Berg, D. A., Skillman, E. D., Croxall, K. V., et al. 2015, ApJ, 806, 16, doi: [10.1088/0004-637X/806/1/16](https://doi.org/10.1088/0004-637X/806/1/16)

Berg, D. A., Skillman, E. D., Garnett, D. R., et al. 2013, *ApJ*, 775, 128, doi: [10.1088/0004-637X/775/2/128](https://doi.org/10.1088/0004-637X/775/2/128)

Berkhuijsen, E. M., & Fletcher, A. 2008, *MNRAS*, 390, L19, doi: [10.1111/j.1745-3933.2008.00526.x](https://doi.org/10.1111/j.1745-3933.2008.00526.x)

Bunker, A. J., Saxena, A., Cameron, A. J., et al. 2023, *A&A*, 677, A88, doi: [10.1051/0004-6361/202346159](https://doi.org/10.1051/0004-6361/202346159)

Butler, K., & Zeippen, C. J. 1989, *A&A*, 208, 337

Cameron, A. J., Saxena, A., Bunker, A. J., et al. 2023, *A&A*, 677, A115, doi: [10.1051/0004-6361/202346107](https://doi.org/10.1051/0004-6361/202346107)

Campbell, A., Terlevich, R., & Melnick, J. 1986, *MNRAS*, 223, 811, doi: [10.1093/mnras/223.4.811](https://doi.org/10.1093/mnras/223.4.811)

Cardelli, J. A., Clayton, G. C., & Mathis, J. S. 1989, *ApJ*, 345, 245, doi: [10.1086/167900](https://doi.org/10.1086/167900)

Carnall, A. C. 2017, arXiv e-prints, arXiv:1705.05165. <https://arxiv.org/abs/1705.05165>

Cataldi, E., Belfiore, F., Curti, M., et al. 2025, *A&A*, 703, A208, doi: [10.1051/0004-6361/202554843](https://doi.org/10.1051/0004-6361/202554843)

Chen, Y., Jones, T., Sanders, R., et al. 2023, *Nature Astronomy*, 7, 771, doi: [10.1038/s41550-023-01953-7](https://doi.org/10.1038/s41550-023-01953-7)

Croxall, K. V., & Pogge, R. W. 2019, *rwpogge/modsIDL: modsIDL Binocular Release*, v1.0 Zenodo, doi: [10.5281/zenodo.2561424](https://doi.org/10.5281/zenodo.2561424)

Croxall, K. V., Pogge, R. W., Berg, D. A., Skillman, E. D., & Moustakas, J. 2015, *ApJ*, 808, 42, doi: [10.1088/0004-637X/808/1/42](https://doi.org/10.1088/0004-637X/808/1/42)

Croxall, K. V., Pogge, R. W., Berg, D. A., Skillman, E. D., & Moustakas, J. 2016, *ApJ*, 830, 4, doi: [10.3847/0004-637X/830/1/4](https://doi.org/10.3847/0004-637X/830/1/4)

Curti, M., Cresci, G., Mannucci, F., et al. 2017, *MNRAS*, 465, 1384, doi: [10.1093/mnras/stw2766](https://doi.org/10.1093/mnras/stw2766)

Delgado-Ingla, G., Morisset, C., & Stasińska, G. 2014, *MNRAS*, 440, 536, doi: [10.1093/mnras/stu341](https://doi.org/10.1093/mnras/stu341)

DESI Collaboration, Adame, A. G., Aguilar, J., et al. 2024, *AJ*, 167, 62, doi: [10.3847/1538-3881/ad0b08](https://doi.org/10.3847/1538-3881/ad0b08)

Dinerstein, H. L. 1990, in *Astrophysics and Space Science Library*, Vol. 161, *The Interstellar Medium in Galaxies*, ed. J. Thronson, Harley A. & J. M. Shull, 257–285, doi: [10.1007/978-94-009-0595-5_10](https://doi.org/10.1007/978-94-009-0595-5_10)

Eldridge, J. J., & Stanway, E. R. 2009, *MNRAS*, 400, 1019, doi: [10.1111/j.1365-2966.2009.15514.x](https://doi.org/10.1111/j.1365-2966.2009.15514.x)

Eldridge, J. J., Stanway, E. R., Xiao, L., et al. 2017, *PASA*, 34, e058, doi: [10.1017/pasa.2017.51](https://doi.org/10.1017/pasa.2017.51)

Esteban, C., Bresolin, F., García-Rojas, J., & Toribio San Cipriano, L. 2020, *MNRAS*, 491, 2137, doi: [10.1093/mnras/stz3134](https://doi.org/10.1093/mnras/stz3134)

Esteban, C., Bresolin, F., Peimbert, M., et al. 2009, *ApJ*, 700, 654, doi: [10.1088/0004-637X/700/1/654](https://doi.org/10.1088/0004-637X/700/1/654)

Esteban, C., García-Rojas, J., Carigi, L., et al. 2014, *MNRAS*, 443, 624, doi: [10.1093/mnras/stu1177](https://doi.org/10.1093/mnras/stu1177)

Esteban, C., García-Rojas, J., Peimbert, M., et al. 2005, *ApJL*, 618, L95, doi: [10.1086/426889](https://doi.org/10.1086/426889)

Esteban, C., Peimbert, M., García-Rojas, J., et al. 2004, *MNRAS*, 355, 229, doi: [10.1111/j.1365-2966.2004.08313.x](https://doi.org/10.1111/j.1365-2966.2004.08313.x)

Fernández, V., Amorín, R., Firpo, V., & Morisset, C. 2024, *A&A*, 688, A69, doi: [10.1051/0004-6361/202449224](https://doi.org/10.1051/0004-6361/202449224)

Fernández, V., Terlevich, E., Díaz, A. I., Terlevich, R., & Rosales-Ortega, F. F. 2018, *MNRAS*, 478, 5301, doi: [10.1093/mnras/sty1206](https://doi.org/10.1093/mnras/sty1206)

Flury, S. R., Arellano-Córdova, K. Z., Moran, E. C., & Einsig, A. 2025, *MNRAS*, 543, 3367, doi: [10.1093/mnras/staf1615](https://doi.org/10.1093/mnras/staf1615)

Froese Fischer, C., & Tachiev, G. 2004, *Atomic Data and Nuclear Data Tables*, 87, 1, doi: [10.1016/j.adt.2004.02.001](https://doi.org/10.1016/j.adt.2004.02.001)

Froese Fischer, C., Tachiev, G., & Irimia, A. 2006, *Atomic Data and Nuclear Data Tables*, 92, 607, doi: [10.1016/j.adt.2006.03.001](https://doi.org/10.1016/j.adt.2006.03.001)

Galavis, M. E., Mendoza, C., & Zeippen, C. J. 1995, *A&AS*, 111, 347

Garnett, D. R. 1992, *AJ*, 103, 1330, doi: [10.1086/116146](https://doi.org/10.1086/116146)

Garnett, D. R., Kennicutt, Robert C., J., Chu, Y.-H., & Skillman, E. D. 1991, *ApJ*, 373, 458, doi: [10.1086/170065](https://doi.org/10.1086/170065)

Giovanelli, R., Haynes, M. P., Adams, E. A. K., et al. 2013, *AJ*, 146, 15, doi: [10.1088/0004-6256/146/1/15](https://doi.org/10.1088/0004-6256/146/1/15)

Gonzalez-Delgado, R. M., Perez, E., Tenorio-Tagle, G., et al. 1994, *ApJ*, 437, 239, doi: [10.1086/174992](https://doi.org/10.1086/174992)

Götberg, Y., de Mink, S. E., Groh, J. H., Leitherer, C., & Norman, C. 2019, *A&A*, 629, A134, doi: [10.1051/0004-6361/201834525](https://doi.org/10.1051/0004-6361/201834525)

Harris, C. R., Millman, K. J., van der Walt, S. J., et al. 2020, *Nature*, 585, 357, doi: [10.1038/s41586-020-2649-2](https://doi.org/10.1038/s41586-020-2649-2)

Hayes, M. J., Saldana-Lopez, A., Citro, A., et al. 2025, *ApJ*, 982, 14, doi: [10.3847/1538-4357/adaea1](https://doi.org/10.3847/1538-4357/adaea1)

Hovis-Afflerbach, B., Götberg, Y., Schootemeijer, A., et al. 2025, *A&A*, 697, A239, doi: [10.1051/0004-6361/202453185](https://doi.org/10.1051/0004-6361/202453185)

Hsyu, T., Cooke, R. J., Prochaska, J. X., & Bolte, M. 2018, *ApJ*, 863, 134, doi: [10.3847/1538-4357/aad18a](https://doi.org/10.3847/1538-4357/aad18a)

Hsyu, T., Cooke, R. J., Prochaska, J. X., & Bolte, M. 2020, *ApJ*, 896, 77, doi: [10.3847/1538-4357/ab91af](https://doi.org/10.3847/1538-4357/ab91af)

Hudson, C. E., Ramsbottom, C. A., & Scott, M. P. 2012, *ApJ*, 750, 65, doi: [10.1088/0004-637X/750/1/65](https://doi.org/10.1088/0004-637X/750/1/65)

Irimia, A., & Froese Fischer, C. 2005, *PhyS*, 71, 172, doi: [10.1238/Physica.Regular.071a00172](https://doi.org/10.1238/Physica.Regular.071a00172)

Izotov, I. I., Guseva, N. G., Lipovetskii, V. A., Kniazev, A. I., & Stepanian, J. A. 1990, *Nature*, 343, 238, doi: [10.1038/343238a0](https://doi.org/10.1038/343238a0)

Izotov, Y. I., Chaffee, F. H., Foltz, C. B., et al. 1999, *ApJ*, 527, 757, doi: [10.1086/308119](https://doi.org/10.1086/308119)

Izotov, Y. I., Papaderos, P., Guseva, N. G., Fricke, K. J., & Thuan, T. X. 2006a, *A&A*, 454, 137, doi: [10.1051/0004-6361:20065100](https://doi.org/10.1051/0004-6361:20065100)

Izotov, Y. I., Stasińska, G., Meynet, G., Guseva, N. G., & Thuan, T. X. 2006b, *A&A*, 448, 955, doi: [10.1051/0004-6361:20053763](https://doi.org/10.1051/0004-6361:20053763)

Izotov, Y. I., & Thuan, T. X. 2007, *ApJ*, 665, 1115, doi: [10.1086/519922](https://doi.org/10.1086/519922)

Izotov, Y. I., Thuan, T. X., & Guseva, N. G. 2012, *A&A*, 546, A122, doi: [10.1051/0004-6361/201219733](https://doi.org/10.1051/0004-6361/201219733)

Izotov, Y. I., Thuan, T. X., & Guseva, N. G. 2014, *MNRAS*, 445, 778, doi: [10.1093/mnras/stu1771](https://doi.org/10.1093/mnras/stu1771)

Izotov, Y. I., Thuan, T. X., & Guseva, N. G. 2017, *MNRAS*, 471, 548, doi: [10.1093/mnras/stx1629](https://doi.org/10.1093/mnras/stx1629)

Izotov, Y. I., Thuan, T. X., & Guseva, N. G. 2021, *MNRAS*, 508, 2556, doi: [10.1093/mnras/stab2798](https://doi.org/10.1093/mnras/stab2798)

Izotov, Y. I., Thuan, T. X., & Stasińska, G. 2007, *ApJ*, 662, 15, doi: [10.1086/513601](https://doi.org/10.1086/513601)

James, B. L., Tsamis, Y. G., & Barlow, M. J. 2010, *MNRAS*, 401, 759, doi: [10.1111/j.1365-2966.2009.15706.x](https://doi.org/10.1111/j.1365-2966.2009.15706.x)

Kauffmann, G., Heckman, T. M., Tremonti, C., et al. 2003, *MNRAS*, 346, 1055, doi: [10.1111/j.1365-2966.2003.07154.x](https://doi.org/10.1111/j.1365-2966.2003.07154.x)

Kaufman, V., & Sugar, J. 1986, *Journal of Physical and Chemical Reference Data*, 15, 321, doi: [10.1063/1.555775](https://doi.org/10.1063/1.555775)

Kelly, B. C. 2007, *ApJ*, 665, 1489, doi: [10.1086/519947](https://doi.org/10.1086/519947)

Kennicutt, Robert C., J., Bresolin, F., & Garnett, D. R. 2003, *ApJ*, 591, 801, doi: [10.1086/375398](https://doi.org/10.1086/375398)

Kewley, L. J., Dopita, M. A., Leitherer, C., et al. 2013, *ApJ*, 774, 100, doi: [10.1088/0004-637X/774/2/100](https://doi.org/10.1088/0004-637X/774/2/100)

Kewley, L. J., Dopita, M. A., Sutherland, R. S., Heisler, C. A., & Trevena, J. 2001, *ApJ*, 556, 121, doi: [10.1086/321545](https://doi.org/10.1086/321545)

Kewley, L. J., & Ellison, S. L. 2008, *ApJ*, 681, 1183, doi: [10.1086/587500](https://doi.org/10.1086/587500)

Khoram, A. H., & Belfiore, F. 2025, *A&A*, 693, A150, doi: [10.1051/0004-6361/202451980](https://doi.org/10.1051/0004-6361/202451980)

Kisielius, R., Storey, P. J., Ferland, G. J., & Keenan, F. P. 2009, *MNRAS*, 397, 903, doi: [10.1111/j.1365-2966.2009.14989.x](https://doi.org/10.1111/j.1365-2966.2009.14989.x)

Kluyver, T., Ragan-Kelley, B., Pérez, F., et al. 2016, in *Positioning and Power in Academic Publishing: Players, Agents and Agendas*, ed. F. Loizides & B. Schmidt, IOS Press, 87 – 90

Kojima, T., Ouchi, M., Rauch, M., et al. 2020, *ApJ*, 898, 142, doi: [10.3847/1538-4357/aba047](https://doi.org/10.3847/1538-4357/aba047)

Kurichin, O. A., Kislytsyn, P. A., & Ivanchik, A. V. 2021a, *Astronomy Letters*, 47, 674, doi: [10.1134/S1063773721100054](https://doi.org/10.1134/S1063773721100054)

Kurichin, O. A., Kislytsyn, P. A., Klimenko, V. V., Balashev, S. A., & Ivanchik, A. V. 2021b, *MNRAS*, 502, 3045, doi: [10.1093/mnras/stab215](https://doi.org/10.1093/mnras/stab215)

Lamarche, C., Smith, J. D., Kreckel, K., et al. 2022, *ApJ*, 925, 194, doi: [10.3847/1538-4357/ac3b4f](https://doi.org/10.3847/1538-4357/ac3b4f)

Liu, X. W., Luo, S. G., Barlow, M. J., Danziger, I. J., & Storey, P. J. 2001, *MNRAS*, 327, 141, doi: [10.1046/j.1365-8711.2001.04676.x](https://doi.org/10.1046/j.1365-8711.2001.04676.x)

Liu, X. W., Storey, P. J., Barlow, M. J., et al. 2000, *MNRAS*, 312, 585, doi: [10.1046/j.1365-8711.2000.03167.x](https://doi.org/10.1046/j.1365-8711.2000.03167.x)

López-Sánchez, A. R., Dopita, M. A., Kewley, L. J., et al. 2012, *MNRAS*, 426, 2630, doi: [10.1111/j.1365-2966.2012.21145.x](https://doi.org/10.1111/j.1365-2966.2012.21145.x)

López-Sánchez, A. R., & Esteban, C. 2010, *A&A*, 516, A104, doi: [10.1051/0004-6361/200913434](https://doi.org/10.1051/0004-6361/200913434)

Luridiana, V., Morisset, C., & Shaw, R. A. 2012, *IAU Symposium*, 283, 422, doi: [10.1017/S1743921312011738](https://doi.org/10.1017/S1743921312011738)

Luridiana, V., Morisset, C., & Shaw, R. A. 2015, *A&A*, 573, A42, doi: [10.1051/0004-6361/201323152](https://doi.org/10.1051/0004-6361/201323152)

Maiolino, R., & Mannucci, F. 2019, *A&A Rev*, 27, 3, doi: [10.1007/s00159-018-0112-2](https://doi.org/10.1007/s00159-018-0112-2)

Martinez, Z., Berg, D. A., James, B. L., et al. 2025, *ApJ*, 995, 204, doi: [10.3847/1538-4357/ae17c6](https://doi.org/10.3847/1538-4357/ae17c6)

Matsumoto, A., Ouchi, M., Nakajima, K., et al. 2022, *ApJ*, 941, 167, doi: [10.3847/1538-4357/ac9ea1](https://doi.org/10.3847/1538-4357/ac9ea1)

Méndez-Delgado, J. E., Esteban, C., García-Rojas, J., Kreckel, K., & Peimbert, M. 2023a, *Nature*, 618, 249, doi: [10.1038/s41586-023-05956-2](https://doi.org/10.1038/s41586-023-05956-2)

Méndez-Delgado, J. E., Esteban, C., García-Rojas, J., et al. 2023b, *MNRAS*, 523, 2952, doi: [10.1093/mnras/stad1569](https://doi.org/10.1093/mnras/stad1569)

Méndez-Delgado, J. E., Kreckel, K., Esteban, C., et al. 2024, *A&A*, 690, A248, doi: [10.1051/0004-6361/202450928](https://doi.org/10.1051/0004-6361/202450928)

Mendoza, C. 1983, in *IAU Symposium*, Vol. 103, *Planetary Nebulae*, ed. L. H. Aller, 143–172

Mendoza, C., & Zeippen, C. J. 1982, *MNRAS*, 198, 127, doi: [10.1093/mnras/198.1.127](https://doi.org/10.1093/mnras/198.1.127)

Micheva, G., Oey, M. S., Jaskot, A. E., & James, B. L. 2017, *ApJ*, 845, 165, doi: [10.3847/1538-4357/aa830b](https://doi.org/10.3847/1538-4357/aa830b)

Mingozzi, M., James, B. L., Arellano-Córdova, K. Z., et al. 2022, *ApJ*, 939, 110, doi: [10.3847/1538-4357/ac952c](https://doi.org/10.3847/1538-4357/ac952c)

Miranda-Pérez, B. E., & Hidalgo-Gámez, A. M. 2023, *ApJ*, 952, 76, doi: [10.3847/1538-4357/acdb4b](https://doi.org/10.3847/1538-4357/acdb4b)

Morisset, C., Luridiana, V., García-Rojas, J., et al. 2020, *Atoms*, 8, 66, doi: [10.3390/atoms8040066](https://doi.org/10.3390/atoms8040066)

Moustakas, J., Kennicutt, Robert C., J., Tremonti, C. A., et al. 2010, *ApJS*, 190, 233, doi: [10.1088/0067-0049/190/2/233](https://doi.org/10.1088/0067-0049/190/2/233)

Nakajima, K., Ouchi, M., Xu, Y., et al. 2022, *ApJS*, 262, 3, doi: [10.3847/1538-4365/ac7710](https://doi.org/10.3847/1538-4365/ac7710)

Noll, S., Kausch, W., Barden, M., et al. 2012, *A&A*, 543, A92, doi: [10.1051/0004-6361/201219040](https://doi.org/10.1051/0004-6361/201219040)

Pagel, B. E. J., Simonson, E. A., Terlevich, R. J., & Edmunds, M. G. 1992, *MNRAS*, 255, 325, doi: [10.1093/mnras/255.2.325](https://doi.org/10.1093/mnras/255.2.325)

Peimbert, M. 1967, *ApJ*, 150, 825, doi: [10.1086/149385](https://doi.org/10.1086/149385)

Peimbert, M., & Costero, R. 1969, *Boletín de los Observatorios Tonantzintla y Tacubaya*, 5, 3

Peimbert, M., & Torres-Peimbert, S. 1974, *ApJ*, 193, 327, doi: [10.1086/153166](https://doi.org/10.1086/153166)

Peimbert, M., & Torres-Peimbert, S. 1976, *ApJ*, 203, 581, doi: [10.1086/154114](https://doi.org/10.1086/154114)

Pilyugin, L. S., Mattsson, L., Vílchez, J. M., & Cedrés, B. 2009, *MNRAS*, 398, 485, doi: [10.1111/j.1365-2966.2009.15182.x](https://doi.org/10.1111/j.1365-2966.2009.15182.x)

Planck Collaboration, Aghanim, N., Akrami, Y., et al. 2020, *A&A*, 641, A6, doi: [10.1051/0004-6361/201833910](https://doi.org/10.1051/0004-6361/201833910)

Pogge, R. 2019, *rwpogge/modsCCDRed*: v2.0.1, 2.0.1 Zenodo, doi: [10.5281/zenodo.2647501](https://doi.org/10.5281/zenodo.2647501)

Pogge, R. W., Atwood, B., Brewer, D. F., et al. 2010, in Society of Photo-Optical Instrumentation Engineers (SPIE) Conference Series, Vol. 7735, Ground-based and Airborne Instrumentation for Astronomy III, ed. I. S. McLean, S. K. Ramsay, & H. Takami, 77350A, doi: [10.1117/12.857215](https://doi.org/10.1117/12.857215)

Prochaska, J. X., Hennawi, J. F., Westfall, K. B., et al. 2020, Journal of Open Source Software, 5, 2308, doi: [10.21105/joss.02308](https://doi.org/10.21105/joss.02308)

Prochaska, J. X., Hennawi, J., Cooke, R., et al. 2020, pypeit/PypeIt: Release 1.0.0, v1.0.0 Zenodo, doi: [10.5281/zenodo.3743493](https://doi.org/10.5281/zenodo.3743493)

Ramsbottom, C. A., & Bell, K. L. 1997, Atomic Data and Nuclear Data Tables, 66, 65, doi: [10.1006/adnd.1997.0741](https://doi.org/10.1006/adnd.1997.0741)

Reynolds, R. J. 1991, ApJL, 372, L17, doi: [10.1086/186013](https://doi.org/10.1086/186013)

Rickards Vaught, R. J., Sandstrom, K. M., Belfiore, F., et al. 2024, ApJ, 966, 130, doi: [10.3847/1538-4357/ad303c](https://doi.org/10.3847/1538-4357/ad303c)

Rickards Vaught, R. J., Hunt, L. K., Aloisi, A., et al. 2025, ApJ, 990, 111, doi: [10.3847/1538-4357/adf10f](https://doi.org/10.3847/1538-4357/adf10f)

Roberts-Borsani, G., Treu, T., Shapley, A., et al. 2024, ApJ, 976, 193, doi: [10.3847/1538-4357/ad85d3](https://doi.org/10.3847/1538-4357/ad85d3)

Rodríguez, M. 2020, MNRAS, 495, 1016, doi: [10.1093/mnras/staa1286](https://doi.org/10.1093/mnras/staa1286)

Rogers, N., et al. 2026,

Rogers, N. S. J., Skillman, E. D., Pogge, R. W., et al. 2022, ApJ, 939, 44, doi: [10.3847/1538-4357/ac947d](https://doi.org/10.3847/1538-4357/ac947d)

Rogers, N. S. J., Skillman, E. D., Pogge, R. W., et al. 2021, ApJ, 915, 21, doi: [10.3847/1538-4357/abf8b9](https://doi.org/10.3847/1538-4357/abf8b9)

Rogers, N. S. J., Strom, A. L., Rudie, G. C., et al. 2024, ApJL, 964, L12, doi: [10.3847/2041-8213/ad2f37](https://doi.org/10.3847/2041-8213/ad2f37)

Rogers, N. S. J., Strom, A. L., Rudie, G. C., et al. 2025, arXiv e-prints, arXiv:2509.18257, doi: [10.48550/arXiv.2509.18257](https://doi.org/10.48550/arXiv.2509.18257)

Rubin, R. H. 1986, ApJ, 309, 334, doi: [10.1086/164606](https://doi.org/10.1086/164606)

Rynkun, P., Gaigalas, G., & Jönsson, P. 2019, A&A, 623, A155, doi: [10.1051/0004-6361/201834931](https://doi.org/10.1051/0004-6361/201834931)

Sánchez Almeida, J., Pérez-Montero, E., Morales-Luis, A. B., et al. 2016, ApJ, 819, 110, doi: [10.3847/0004-637X/819/2/110](https://doi.org/10.3847/0004-637X/819/2/110)

Sanders, R. L., Shapley, A. E., Kriek, M., et al. 2016, ApJ, 816, 23, doi: [10.3847/0004-637X/816/1/23](https://doi.org/10.3847/0004-637X/816/1/23)

Sanders, R. L., Shapley, A. E., Topping, M. W., et al. 2025, arXiv e-prints, arXiv:2508.10099, doi: [10.48550/arXiv.2508.10099](https://doi.org/10.48550/arXiv.2508.10099)

Scholte, D., Cullen, F., Moustakas, J. M., et al. 2026, arXiv e-prints, arXiv:2601.02463, doi: [10.48550/arXiv.2601.02463](https://doi.org/10.48550/arXiv.2601.02463)

Searle, L., & Sargent, W. L. W. 1972, ApJ, 173, 25, doi: [10.1086/151398](https://doi.org/10.1086/151398)

Senchyna, P., Stark, D. P., Mirocha, J., et al. 2020, MNRAS, 494, 941, doi: [10.1093/mnras/staa586](https://doi.org/10.1093/mnras/staa586)

Senchyna, P., Stark, D. P., Vidal-García, A., et al. 2017, MNRAS, 472, 2608, doi: [10.1093/mnras/stx2059](https://doi.org/10.1093/mnras/stx2059)

Shapley, A. E., Reddy, N. A., Kriek, M., et al. 2015, ApJ, 801, 88, doi: [10.1088/0004-637X/801/2/88](https://doi.org/10.1088/0004-637X/801/2/88)

Shapley, A. E., Sanders, R. L., Topping, M. W., et al. 2025, ApJ, 980, 242, doi: [10.3847/1538-4357/adad68](https://doi.org/10.3847/1538-4357/adad68)

Shirazi, M., & Brinchmann, J. 2012, MNRAS, 421, 1043, doi: [10.1111/j.1365-2966.2012.20439.x](https://doi.org/10.1111/j.1365-2966.2012.20439.x)

Skillman, E., et al. 2026,

Skillman, E. D. 1985, ApJ, 290, 449, doi: [10.1086/163003](https://doi.org/10.1086/163003)

Skillman, E. D., Berg, D. A., Pogge, R. W., et al. 2020, ApJ, 894, 138, doi: [10.3847/1538-4357/ab86ae](https://doi.org/10.3847/1538-4357/ab86ae)

Skillman, E. D., & Kennicutt, Jr., R. C. 1993, ApJ, 411, 655, doi: [10.1086/172868](https://doi.org/10.1086/172868)

Skillman, E. D., Salzer, J. J., Berg, D. A., et al. 2013, AJ, 146, 3, doi: [10.1088/0004-6256/146/1/3](https://doi.org/10.1088/0004-6256/146/1/3)

Stanway, E. R., & Eldridge, J. J. 2018, MNRAS, 479, 75, doi: [10.1093/mnras/sty1353](https://doi.org/10.1093/mnras/sty1353)

Storey, P. J., & Hummer, D. G. 1995, MNRAS, 272, 41, doi: [10.1093/mnras/272.1.41](https://doi.org/10.1093/mnras/272.1.41)

Storey, P. J., Sochi, T., & Badnell, N. R. 2014, MNRAS, 441, 3028, doi: [10.1093/mnras/stu777](https://doi.org/10.1093/mnras/stu777)

Strom, A. L., Steidel, C. C., Rudie, G. C., et al. 2017, ApJ, 836, 164, doi: [10.3847/1538-4357/836/2/164](https://doi.org/10.3847/1538-4357/836/2/164)

Tayal, S. S. 2011, ApJS, 195, 12, doi: [10.1088/0067-0049/195/2/12](https://doi.org/10.1088/0067-0049/195/2/12)

Tayal, S. S., & Zatsarinsky, O. 2010, ApJS, 188, 32, doi: [10.1088/0067-0049/188/1/32](https://doi.org/10.1088/0067-0049/188/1/32)

Thuan, T. X., Izotov, Y. I., & Lipovetsky, V. A. 1995, ApJ, 445, 108, doi: [10.1086/175676](https://doi.org/10.1086/175676)

Topping, M. W., Stark, D. P., Senchyna, P., et al. 2024, MNRAS, 529, 3301, doi: [10.1093/mnras/stae682](https://doi.org/10.1093/mnras/stae682)

Topping, M. W., Sanders, R. L., Shapley, A. E., et al. 2025, MNRAS, 541, 1707, doi: [10.1093/mnras/staf903](https://doi.org/10.1093/mnras/staf903)

Toribio San Cipriano, L., García-Rojas, J., Esteban, C., Bresolin, F., & Peimbert, M. 2016, MNRAS, 458, 1866, doi: [10.1093/mnras/stw397](https://doi.org/10.1093/mnras/stw397)

van Dokkum, P. G. 2001, PASP, 113, 1420, doi: [10.1086/323894](https://doi.org/10.1086/323894)

Veilleux, S., & Osterbrock, D. E. 1987, ApJS, 63, 295, doi: [10.1086/191166](https://doi.org/10.1086/191166)

Virtanen, P., Gommers, R., Oliphant, T. E., et al. 2020, Nature Methods, 17, 261, doi: [10.1038/s41592-019-0686-2](https://doi.org/10.1038/s41592-019-0686-2)

Watanabe, K., Ouchi, M., Nakajima, K., et al. 2024, ApJ, 962, 50, doi: [10.3847/1538-4357/ad13ff](https://doi.org/10.3847/1538-4357/ad13ff)

Welch, B., Rivera-Thorsen, T. E., Rigby, J. R., et al. 2025, ApJ, 980, 33, doi: [10.3847/1538-4357/ada76c](https://doi.org/10.3847/1538-4357/ada76c)

Weller, M., et al. 2026,

Weller, M. K., Weinberg, D. H., & Johnson, J. W. 2025, MNRAS, 538, 1517, doi: [10.1093/mnras/staf373](https://doi.org/10.1093/mnras/staf373)

Wofford, A., Vidal-García, A., Feltre, A., et al. 2021, MNRAS, 500, 2908, doi: [10.1093/mnras/staa3365](https://doi.org/10.1093/mnras/staa3365)

Yates, R. M., Schady, P., Chen, T. W., Schweyer, T., & Wiseman, P. 2020, A&A, 634, A107, doi: [10.1051/0004-6361/201936506](https://doi.org/10.1051/0004-6361/201936506)